BIOMIMETICS

Kirigami skins make a simple soft actuator crawl

Ahmad Rafsanjani, Yuerou Zhang, Bangyuan Liu, Shmuel M. Rubinstein, Katia Bertoldi*

Bioinspired soft machines made of highly deformable materials are enabling a variety of innovative applications, yet their locomotion typically requires several actuators that are independently activated. We harnessed kirigami principles to significantly enhance the crawling capability of a soft actuator. We designed highly stretchable kirigami surfaces in which mechanical instabilities induce a transformation from flat sheets to 3D-textured surfaces akin to the scaled skin of snakes. First, we showed that this transformation was accompanied by a dramatic change in the frictional properties of the surfaces. Then, we demonstrated that, when wrapped around an extending soft actuator, the buckling-induced directional frictional properties of these surfaces enabled the system to efficiently crawl.

INTRODUCTION

Nature offers many examples of slender limbless organisms that take advantage of both the flexibility of their body and the frictional properties of their skin to efficiently move and explore the surrounding space (*1–5*). For example, snakes rely on the substantial reconfiguration in the shape of their body (*6*) and on the frictional anisotropy of their skin (*7*) to propel themselves. Not only microscopic features (*8*, *9*) but also the macroscale structure and arrangement of their ventral scales contribute to such anisotropic friction (*5*), because their preferred orientation makes sliding in the forward direction much easier than in the backward one.

The flexibility of soft-bodied animals has recently inspired the design of new class of soft robots that are easy and inexpensive to fabricate yet still can achieve complex motions (*10–14*). However, efforts to replicate natural frictional properties in synthetic systems have been limited (*15*, *16*). The skin of the vast majority of soft robots consists of an unstructured flexible membrane that lacks directional frictional properties. As a result, multiple actuators activated independently are typically required to achieve locomotion (*16–21*).

Inspired by the friction-assisted locomotion of snakes (*1*, *5*, *7*) and by the recent advances in engineered surfaces with programmable tribological behavior (*22–25*), we introduce here a smart and flexible skin with anisotropic frictional properties that enables a single soft actuator to propel itself. To this end, we took advantage of kirigami, the ancient Japanese art of paper cutting, whose principles have recently emerged as promising tools to realize highly stretchable and morphable structures (*26–29*). We realized the skin by embedding an array of properly designed cuts into a planar plastic sheet (Fig. 1A) and then wrapping it around a soft actuator (see Fig. 1, B to D). Upon inflation, the elongation of the actuator triggered a mechanical instability in the kirigami skin that in turn induced the pop-up of a three-dimensional (3D) morphology similar to that of a snake's skin (Fig. 1, E and F). The highly directional 3D features induced by buckling significantly altered the frictional properties of the kirigami skins and enabled our simple machine to move forward. The buckling-induced pop-up process observed in our kirigami skin resembles the ability of the snakes to actively actuate their scales (Fig. 1F and movie S1) to tune their frictional properties (*5*).

RESULTS

We considered a soft fluidic actuator comprising an elastomeric tube made of silicone rubber (Smooth-On Inc., Ecoflex 00-30; shear modulus $\mu_a \simeq 30$ kPa) with a length of 164 mm and a triangular cross section with edges of 25 mm (see Fig. 1, B and C). To maximize its elongation during inflation and constrain any other mode of deformation, we surrounded the tube with stiff Kevlar fibers arranged in a helical pattern with small pitch (so that the fibers were almost aligned with the circumferential direction—see the Supplementary Materials for details). We found that the actuator extended by 25% when inflated with a maximum volume of V_{max} = 24 ml of air. However, because symmetry resulted in equal movements of both actuator ends during inflation and deflation, this system did not move forward when placed on a substrate (see movie S2).

Next, we covered the actuator with kirigami skins (see Fig. 1D and movie S3) and investigated their effect on its ability to move. Our kirigami skins were fabricated by laser cutting 9 by 32 centimeter-scale unit cells arranged on a triangular lattice with spacing of l = 4.5 mm and hinge width of δ = 0.7 mm into polyester plastic sheets (Artus Corporation; Young's modulus of E = 4.33 GPa, see fig. S2). Inspired by the shapes observed in ventral scales of snakes (*22*), we considered four different cuts (see Fig. 2A): (i) linear cuts, (ii) triangular cuts, (iii) circular cuts, and (iv) trapezoidal cuts. For all assembled kirigami-skinned crawlers, we first characterized their elongation (ε) and pressure (P) as a function of the supplied volume (V) and then investigated how inflation affected the frictional force when they moved on a substrate. To this end, we pulled (i.e., moved backward) and pushed (i.e., moved forward) the crawlers inflated by different amounts of air against a rough surface (polyurethane foam) while monitoring the resistive force (F_{fr}). Effective coefficients of friction in backward (μ_b) and forward (μ_f) directions were then extracted from these measurements as

$$\mu_b = \frac{\left\langle F_b^{peak} \right\rangle}{F_N}, \quad \mu_f = \frac{\left\langle F_f^{peak} \right\rangle}{F_N} \tag{1}$$

where $F_N \simeq 0.2$ N is the crawler's weight, $\langle \cdot \rangle$ denotes the mean value, and F_b^{peak} and F_f^{peak} are the local peaks of F_{fr} recorded during pulling and pushing, respectively (see the Supplementary Materials for details).

Although the pattern with linear cuts has been used frequently to design highly stretchable systems (*26*, *29*), we found that the corresponding kirigami skin severely limited the extensibility of the actuator [i.e., $\varepsilon = (L - L_0)/L_0 < 0.05$, L_0, and L denoting the undeformed and deformed lengths of the perforated part of the skin (Fig. 2B)] and made it very stiff (see Fig. 2C). This is because the antisymmetric out-of-plane buckling mode typical of this kirigami sheet is characterized by alternating up and down (see fig. S6B) buckled ligaments (*26*) and therefore is suppressed by the presence of the actuator. Hence, no features pop up upon inflation (see inset in Fig. 2F), the crawler slides

John A. Paulson School of Engineering Applied Sciences, Harvard University, Cambridge, MA 02138, USA.
*Corresponding author. Email: bertoldi@seas.harvard.edu

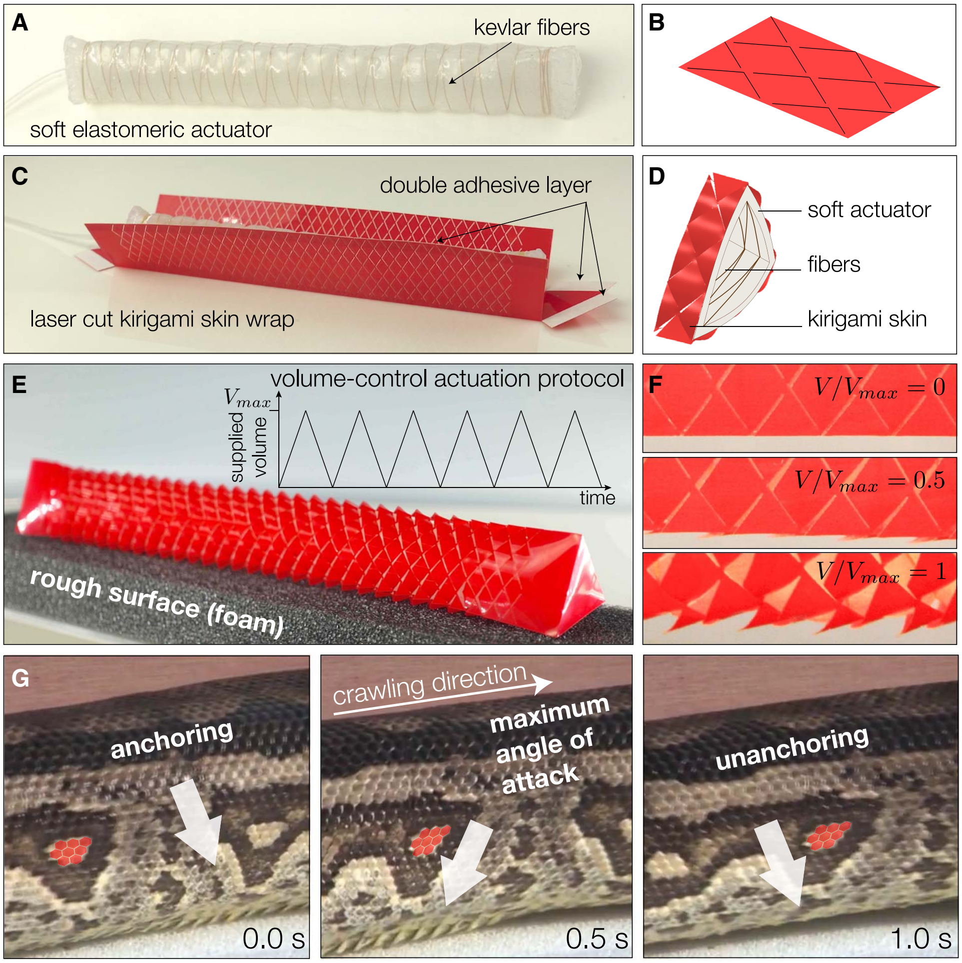

Fig. 1. Kirigami-skinned soft crawlers. (**A**) We considered a fiber-reinforced elastomeric soft actuator that extends axially upon inflation. (**B**) A kirigami skin was fabricated by embedding an array of cuts into a thin plastic sheet. (**C**) A kirigami-skinned soft crawler was built by wrapping the kirigami skin around the actuator. (**D**) Cross-sectional view of a kirigami-skinned soft crawler. (**E**) Inflation of the actuator resulted in a buckling-induced pop-up texture similar to that of a snake's skin. Inset: A typical volume-control actuation protocol with a maximum volume V_{max}. (**F**) Close-up views of a kirigami skin with triangular cuts at a different level of supplied volume V (note that V_{max} = 24 ml is the maximum supplied volume). (**G**) Snapshots showing the rectilinear gait of a female Dumeril's boa (*Acrantophis dumerili*). The snake actively tilts the ventral scales to increase frictional anisotropy and enhance anchoring (video courtesy of H. Marvi and D. Hu).

backward directions, and $\mu_b \simeq \mu_f \simeq 1 \sim 1.5$ for all three systems (the slight increase in μ_b and μ_f compared to the case of the skin with linear cuts was due to the sharper features of the cuts). However, above the instability threshold (i.e., for supplied volume ratios $V/V_{max} > 0.25$), the popping out of the features defined by the cuts led to a jerking motion in backward direction, with the crawlers that alternatively stuck to the substrate and slid over it. This stick-slip regime was also apparent from the measured frictional force, which presented a discrete sequence of sharp drops (see Fig. 2E). Moreover, the instability-induced pop-up process resulted in a significant increase of the magnitude of F_{fr} measured during pulling (see Fig. 2E) so that $\mu_b >> \mu_f$ for supplied volume ratios $V/V_{max} > 0.25$. Therefore, our results indicate that buckling can be exploited to transform the frictional properties of a surface from isotropic to highly anisotropic. However, for this transformation to happen, it is necessary that all features pop up in the same direction (i.e., toward the crawlers' tail). To demonstrate this important point, we considered a kirigami skin with half of the triangular cuts pointing to the head of the crawler and the remaining pointing to its tail (we refer to this pattern as the mirrored triangular pattern). In this case, buckling triggered a pop-up process, and the symmetry of the resulting 3D pattern induced a significant increase of both μ_f and μ_b and did not introduce any frictional directionality (i.e., $\mu_b \sim \mu_f$, see fig. S6C).

Having characterized the tribological behavior of our kirigami-skinned crawlers, we then investigated how friction affected their ability to crawl. To this end, we monitored the position of the crawlers

smoothly in both directions, and the frictional force recorded during pulling and pushing reaches similar values, which are not affected by the supplied volume V (see red lines in Fig. 2, D and E), yielding $\mu_f(V) \simeq \mu_b(V) \simeq 0.75 - 1$ (see Fig. 2F).

By contrast, we found that the other three skins only moderately limited the extensibility of the soft actuator (i.e., $\varepsilon \simeq 0.12 \sim 0.18$, see Fig. 2B) and resulted in a pressure-elongation curve characterized by an initial linear regime, a pressure plateau, and a final stiffening. While in the initial linear regime, all hinges bent in-plane, and the skins remained flat; the sudden departure from linearity to a plateau stress was caused by the out-of-plane buckling of the hinges, which induced the formation of a 3D pattern similar to that of a snake's skin with all features homogeneously popping outward (see insets in Fig. 2, G to I, and fig. S8). This buckling-induced pop-up significantly altered the measured frictional force. Before the instability (i.e., for supplied volume ratios $V/V_{max} < 0.25$), the crawlers slid smoothly in both forward and

placed on a rough surface (polyurethane foam) as they were inflated by supplying a volume of air V_{max} = 24 ml and deflated by extracting the same amount of fluid at a rate of 300 ml/min (see movie S4). In Fig. 3A, we overlay initial and final positions of the crawlers after six inflation cycles, whereas in Fig. 3B, we report the evolution of the displacement of their centers of mass (solid lines), tails (dashed lines), and heads (dotted lines). These results indicate that the crawlers with kirigami skins exhibiting directional frictional properties (i.e., those with circular, triangular, and trapezoidal cuts) were capable of propelling themselves much more efficiently than the other ones. Specifically, if we indicated with u_{cycle}, the displacement recorded at the end of each cycle, then we found that u_{cycle}/L_0 = 0, 0.015, 0.068, 0.08, and 0.12 for the kirigami-skinned crawlers with linear, mirrored triangular, triangular, circular, and trapezoidal cuts, respectively. Although the poor performance of the kirigami-skinned crawler with linear cuts can be attributed to its very limited extensibility, the very short distance traveled by the crawler

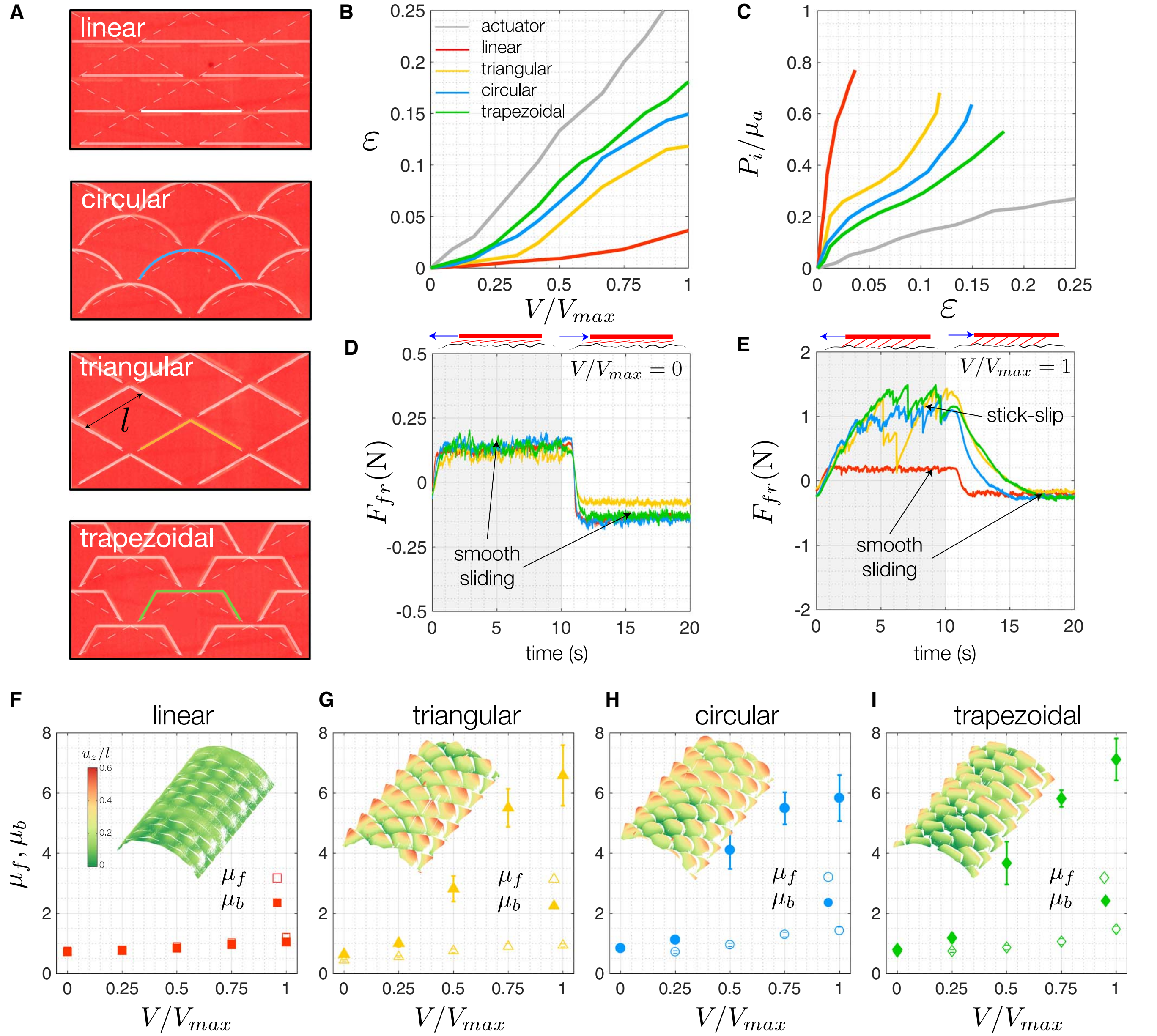

Fig. 2. Characterization of kirigami-skinned soft crawlers. (**A**) Cut shapes considered in this study. (**B**) Elongation of the crawlers as a function of their volume. (**C**) Pressure normalized by the shear modulus of actuator μ_a versus axial strain for the kirigami-skinned crawlers. (**D** and **E**) Friction force F_{fr} measured in backward and forward directions at supplied volumes (D) $V/V_{max} = 0$ and (E) $V/V_{max} = 1$ (with a maximum volume $V_{max} = 24$ ml). (**F** to **I**) Effective coefficients of friction versus inflation levels in forward (hollow symbols) and backward (filled symbols) directions with (F) linear, (G) triangular, (H) circular, and (I) trapezoidal cuts. Insets: 3D-scanned surface profiles of the skins at the supplied volume $V/V_{max} = 1$.

with the mirrored triangular cuts points to the importance of the anisotropic frictional properties introduced by the buckled kirigami skins. Last, we note that the efficiency of our kirigami-skinned crawlers with anisotropic frictional properties (i.e., those with triangular, circular, and trapezoidal cuts) was mainly determined by the stretchability of their skin. The skin with trapezoidal cuts was more stretchable than those with circular and triangular cuts and, therefore, enabled the crawler to have a longer stride and move further.

To further understand how the frictional properties of our kirigami skins affect locomotion, we focused on the position of the anchor point (x_a) at which the crawlers gripped the substrate (i.e., the instantaneous stagnation point along the crawler body) to pull themselves forward and prevent backward sliding (6). By balancing the frictional forces exerted by the substrate on the skin (while neglecting inertial forces due to the slow nature of the crawling motion), we show that (see the Supplementary Materials for details)

$$\left(\frac{x_a}{L}\right)_{\text{inflation}} = \frac{1}{2}\left(\frac{\mu_f - \mu_b}{\mu_f + \mu_b}\right), \quad \left(\frac{x_a}{L}\right)_{\text{deflation}} = \frac{1}{2}\left(\frac{\mu_b - \mu_f}{\mu_f + \mu_b}\right) \tag{2}$$

which provides explicit relations between the position of the anchor point and the frictional properties of the kirigami skin. Equation 2

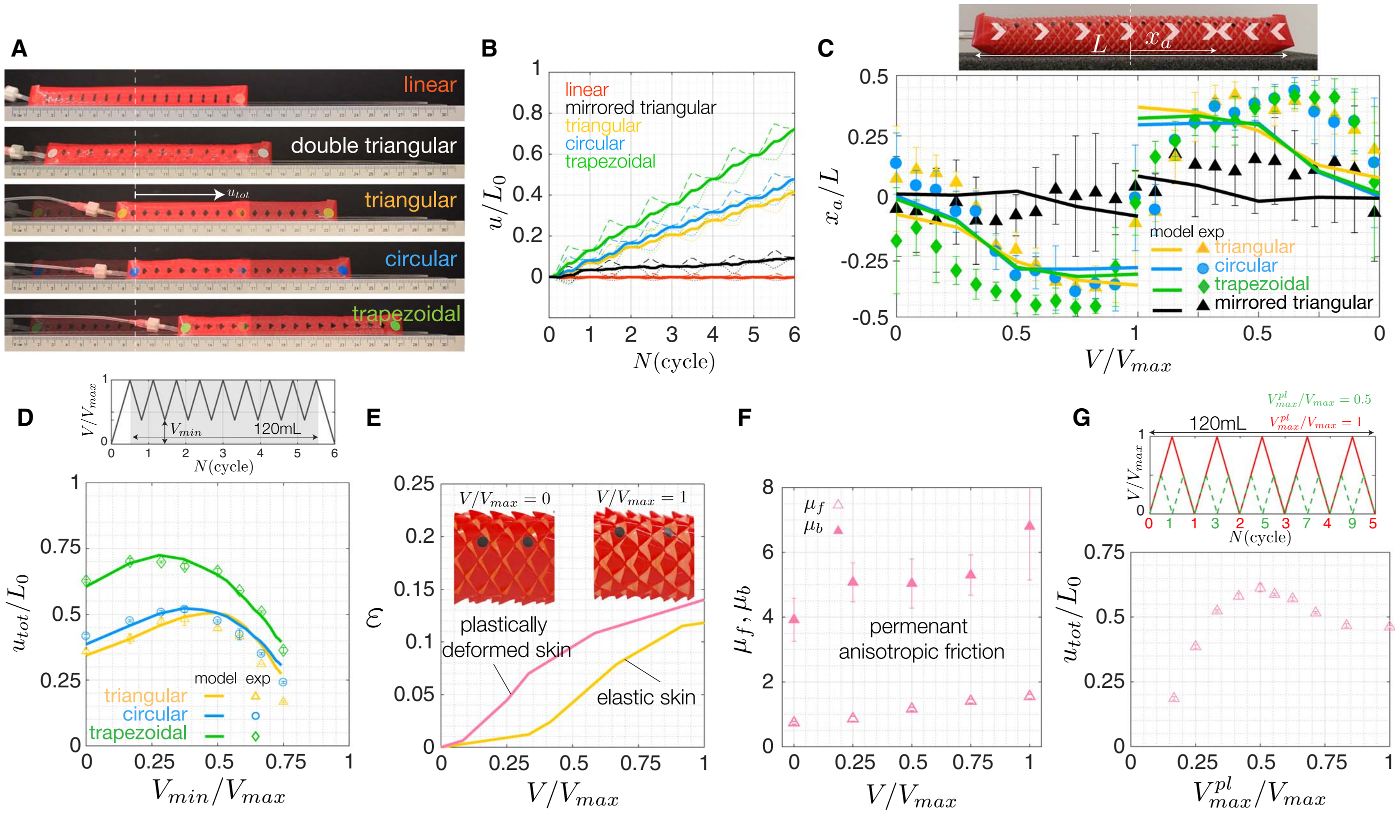

Fig. 3. Crawler locomotion. (**A**) Initial and final position of the crawlers after six inflation cycles with $V \in [0,24]$ ml. (**B**) Displacement of the center of mass (solid line), head (dashed line), and tail (dotted line) of the crawlers versus number of cycles. (**C**) Position of the anchor point during inflation and deflation. The markers denote the experimental data over six cycles. The solid lines denote the predictions given by Eq. 2 using the experimentally measured friction coefficients. (**D**) Measured (markers) and predicted (continuous lines) total displacement when a volume of 120 ml of air was supplied by cyclically inflating and deflating the actuators between V_{max} = 24 ml and $V_{min} \in [0,V_{max}]$. (**E**) Elongation versus supplied volume for a kirigami-skinned crawler with triangular cuts. Results for elastic (yellow line) and plastically deformed (purple line) skins are compared. The inset shows the plastically deformed skin at V/V_{max} = 0 and 1 (with V_{max} = 24 ml). (**F**) Effective coefficients of friction versus supplied volume for the crawler with the plastically deformed skin. (**G**) Measured total displacement for the crawler with the plastically deformed skin when a volume of 120 ml of air was supplied by cyclically inflating and deflating it between 0 ml and V^{pl}_{max}, with $V^{pl}_{max} \in [0,24]$ ml. Error bars indicate SD of the measured anchor points during six inflation/deflation cycles.

indicates that, to maximize the distance traveled by the crawlers, the ratio μ_b/μ_f should be as large as possible. In this case, x_a/L approaches ±0.5, and anchoring occurs at the tail during inflation/elongation and at the head during deflation/shortening, completely preventing backward sliding. Moreover, Eq. 2 also shows that for $\mu_b \sim \mu_f$, the anchor point is located at the center of mass of the crawlers (i.e., $x_a/L \sim 0$). In this case, the head and tail of the crawlers move by the same amount (but in opposite directions) during inflation and deflation, and there is no advancement. In Fig. 3C, we compared the position of the anchor point extracted by our tests with that predicted by Eq. 2 using the experimentally measured friction coefficients reported in Fig. 2 (F to I). We found that the trends observed in our experiments are well captured by our simple model. When the kirigami skin has isotropic frictional properties (as for the patterns with mirrored triangular cuts during the entire inflation/deflation process and with circular, triangular, and trapezoidal cuts before buckling), then x_a/L is about 0. By contrast, if $\mu_b >> \mu_f$ (as for the skins with triangular, circular, and trapezoidal cuts after buckling), then the anchor point moves toward the tail and the head of the crawler during inflation and deflation, respectively.

The results reported in Fig. 3 (A to C) show that, by taking advantage of the directional frictional properties induced in the kirigami skins by buckling, even a single soft actuator can propel itself. They also indicate that the conditions used in our experiments were not optimal, because even for our best kirigami-skinned crawlers, the anchor points were located near their centers of mass for volume ratios $V/V_{max} < 0.25$. This limitation can be overcome by not fully deflating the actuators so that they always operate in the region where the skin has anisotropic frictional properties. In Fig. 3E, we report the measured (markers) and predicted (continuous lines) total displacement (u_{tot}) when a total volume V_{tot} = 120 ml of air was supplied by cyclically inflating and deflating them between the maximum volume V_{max} = 24 ml and the minimum volume $V_{min} \in [0,V_{max}]$ (see movie S5 and the Supplementary Materials for details). We found that there is an optimum value of the minimum volume V_{min} for which the crawlers move more efficiently. Whereas for smaller values of the minimum volume V_{min}, the lack of anisotropic frictional properties resulted in smaller total displacement u_{tot}, when V_{min} was increased above the optimum value, the limited change in length experienced by the crawlers during the cycles became the limiting factor.

To date, we have considered kirigami skins that were initially flat and in which buckling induced the reversible and repeatable formation of a 3D directional texture, but plastic deformation at the ligaments can also be harnessed to generate a permanent 3D morphology

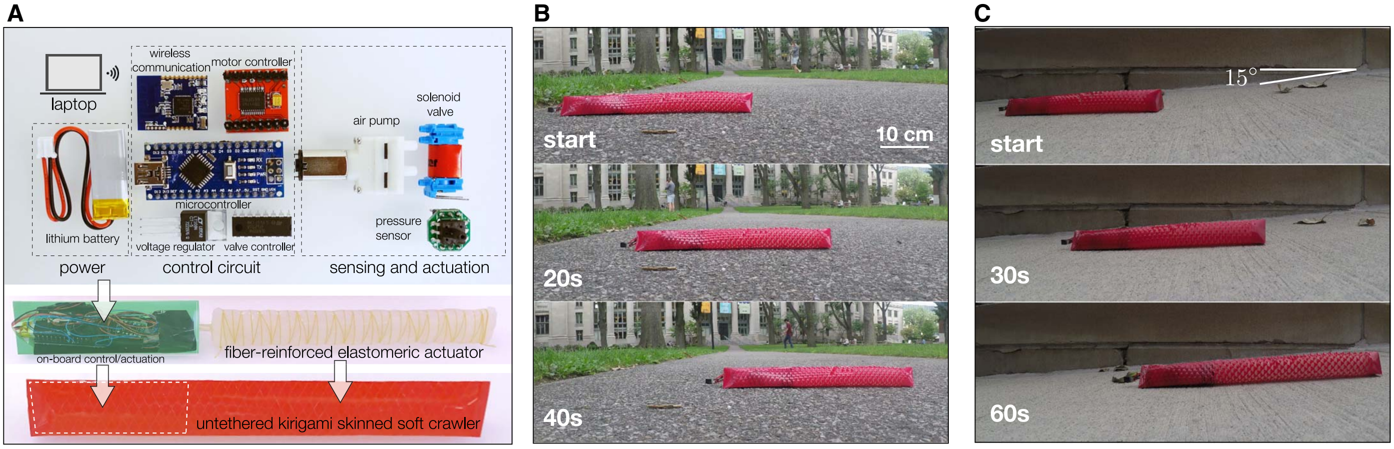

Fig. 4. Untethered kirigami-skinned soft crawlers. (**A**) Fabrication of our untethered kirigami-skinned crawlers. (**B**) Untethered kirigami-skinned soft crawler with circular cuts moves over asphalt. (**C**) Untethered kirigami-skinned soft crawler with trapezoidal cuts climbs a concrete ramp.

(*28*) and, therefore, to improve the efficiency of the crawlers. To demonstrate this, we considered a kirigami skin with triangular cuts, and before wrapping it around the actuators, we applied a large stretch so that in the post-buckling regime, plastic strains developed in the ligament between the cuts, creating a permanent pop-up pattern (see insets of Fig. 3E). We found that this plastically deformed skin affected the response of the system in two ways. On the one hand, it increased the elongation that the crawler experienced at the beginning of the inflation process (Fig. 3E). On the other hand, its permanent directional texture resulted in highly anisotropic frictional properties through the entire actuation process (Fig. 3F). Hence, the efficiency in locomotion for this crawler was optimal when the supplied volume was cyclically varied between 0 and 12 ml (Fig. 3G), resulting in ~22% improvement in comparison to the best performance of the corresponding crawler with a purely elastic kirigami skin.

CONCLUSION

In summary, we have demonstrated that kirigami principles can be exploited to create bioinspired flexible and morphable skins with directional frictional properties that can be integrated in soft robots to achieve locomotion even with a single extending actuator. Although several techniques (including rapid prototyping, pop-up fabrication, and origami) have been proposed to fabricate morphable structures in the recent years, we believe that the proposed kirigami approach provides a simpler, faster, and cheaper technique to create them. Our kirigami skins were fabricated by simply embedding an array of cuts into a planar thin sheet. Mechanical instabilities triggered under uniaxial tension were then exploited to create a 3D pattern and even to guide the formation of permanent folds.

We have shown that the efficiency of our kirigami-skinned crawlers can be improved by properly balancing the frictional properties and stretchability of the skins through careful choice of the cut geometry and the actuation protocol. Moreover, our results indicate that the plastic deformation at the hinges can be harnessed to further optimize the response of the system. However, the reversible and repeatable pop-up process observed in the elastic regime offers opportunities for on-demand and active control of friction, which is important for a broad range of applications, including robotic manipulation and transfer printing (*23*). Although we have focused on fluid-driven soft actuators in this study, the designed stretchable kirigami skins can also be applied to different classes of soft robots, including those based on dielectric elastomers (*30*, *31*), shape memory polymers (*32*), shape memory alloys (*15*, *20*, *21*), and hydrogels (*33*). In addition, because the properties of the designed kirigami skins are primarily governed by the geometry of the structure rather than the constitutive properties of the material, the proposed principles can be applied to systems over a wide range of length scales and made of different materials. Hence, recent advances in top-down techniques, such as photolithography (*26*), open up exciting opportunities for miniaturization of the proposed architectures. On the other side, thicker and stiffer sheets can be used to realize skins for larger robots such as planetary rovers for space exploration.

Last, we note that all crawlers considered in this study were actuated pneumatically using air transferred to them from a stationary source via a flexible tube. However, real-world applications require systems that are capable of operating without the constraint of a tether. As a first step in this direction, we built a fully untethered kirigami-skinned soft crawler by integrating on-board control, sensing, actuation, and power supply (Fig. 4A, see the Supplementary Materials for details). Because all these components can be packed into a volume as small as 25 mm^3 and as light as 45 g, they can be attached to the tail of the actuator without limiting its ability to move on a variety of terrains (Fig. 4, B and C, movies S6 to S10, and fig. S13). Hence, we believe that our kirigami-based strategy opens avenues for the design of new class of soft crawlers that can travel across complex environments for search and rescue, exploration and inspection operations, environmental monitoring, and medical procedures.

MATERIALS AND METHODS

Fabrication of kirigami-skinned crawlers

The kirigami-skinned soft crawlers investigated in this study comprised a fiber-reinforced soft actuator wrapped with a kirigami sheet. The fiber-reinforced soft actuators were made by pouring a platinum-catalyzed silicone rubber (Ecoflex 00-30, Smooth-On Inc.) into a 3D-printed mold. The actuator has a hollow prismatic tube with a triangular cross section. To maximize the elongation of the actuator upon inflation and constrain its deformation in the circumferential direction, we surrounded the elastomeric tube by stiff Kevlar fibers arranged in a helical pattern. The fibers were held in place by brushing the surface of the actuator with a very thin layer of uncured elastomer. The kirigami skins were fabricated by laser cutting an array of 9 by 32 unit cells into 51-μm thick polyester plastic sheets (Artus Corporation, NJ). To assemble the kirigami-skinned crawlers, we wrapped the kirigami sheet around the fiber-reinforced actuator and attached its two edges together using a double-sided adhesive sheet (Blick Art Materials, IL). More details on crawler design, geometry of cuts, fabrication, testing methods, analytical model, and finite-element simulations may be found in the Supplementary Materials.

SUPPLEMENTARY MATERIALS

robotics.sciencemag.org/cgi/content/full/3/15/eaar7555/DC1
Supplementary sections S1 to S4.
Fig. S1. Fabrication of an extending fiber-reinforced actuator.
Fig. S2. Kirigami patterns.
Fig. S3. Fabrication and assembly of kirigami-skinned crawlers.
Fig. S4. Untethered kirigami-skinned crawler.
Fig. S5. Mechanical response of the actuator.
Fig. S6. Mechanical response of kirigami sheets.
Fig. S7. Mechanical response of kirigami-skinned crawlers.
Fig. S8. Evolution of surface morphology for our kirigami-skinned crawlers.
Fig. S9. Friction measurement setup.
Fig. S10. Friction measurements.
Fig. S11. Effective friction coefficients.
Fig. S12. Frictional properties of a crawler with a plastically deformed skin.
Fig. S13. Locomotion of our untethered kirigami-skinned crawler.
Fig. S14. Relation between the location of the anchor point and the fraction coefficients.
Fig. S15. Finite-element simulations of kirigami unit cells.
Movie S1. Rectilinear gait of a female Dumeril's boa.
Movie S2. A fiber-reinforced extending actuator is placed over a rough surface and is subjected to cyclic inflation/deflation.
Movie S3. Assembly of a kirigami-skinned soft crawler.
Movie S4. Motion of the crawlers during six inflation cycles with $V \in [0,24]$ ml.
Movie S5. Motion of the crawlers when a total volume $V_{tot} = 120$ ml of air is supplied by cyclically inflating and deflating them between $V_{max} = 24$ ml and $V_{min} \in [0,V_{max}]$.
Movie S6. Fully untethered kirigami skinned crawlers with triangular, circular, and trapezoidal kirigami skins.
Movie S7. An untethered crawler with circular kirigami skin propels itself over asphalt.
Movie S8. An untethered crawler with trapezoidal kirigami skin climbs a concrete ramp.
Movie S9. An untethered crawler with triangular kirigami skin propels itself over rough stone.
Movie S10. Motion of an untethered crawler with trapezoidal kirigami skin for $P_{min} = 1$, 4, 8, and 12 kPa and $P_{max} = 16$ kPa.
References (*34–38*)

REFERENCES AND NOTES

1. H. W. Lissmann, Rectilinear locomotion in a snake (*Boa occidentalis*). *J. Exp. Biol.* **26**, 368–379 (1950).
2. M. Denny, Locomotion: The cost of gastropod crawling. *Science* **208**, 1288–1290 (1980).
3. D. Berrigan, D. J. Pepin, How maggots move: Allometry and kinematics of crawling in larval Diptera. *J. Insect Physiol.* **41**, 329–337 (1995).
4. R. D. Maladen, Y. Ding, C. Li, D. I. Goldman, Undulatory swimming in sand: Subsurface locomotion of the sandfish lizard. *Science* **325**, 314–318 (2009).
5. H. Marvi, J. P. Cook, J. L. Streator, D. L. Hu, Snakes move their scales to increase friction. *Biotribology* **5**, 52–60 (2016).
6. R. M. Alexander, *Principles of Animal Locomotion* (Princeton Univ. Press, 2006).
7. D. L. Hu, J. Nirody, T. Scott, M. J. Shelley, The mechanics of slithering locomotion. *Proc. Natl. Acad. Sci. U.S.A.* **106**, 10081–10085 (2009).
8. J. Hazel, M. Stone, M. S. Grace, V. V. Tsukruk, Nanoscale design of snake skin for reptation locomotions via friction anisotropy. *J. Biomech.* **32**, 477–484 (1999).
9. R. A. Berthé, G. Westhoff, H. Bleckmann, S. N. Gorb, Surface structure and frictional properties of the skin of the Amazon tree boa *Corallus hortulanus* (Squamata, Boidae). *J. Comp. Physiol. A* **195**, 311–318 (2009).
10. D. Trivedi, C. D. Rahn, W. M. Kier, I. D. Walker, Soft robotics: Biological inspiration, state of the art, and future research. *Appl. Bionics Biomech.* **5**, 99–117 (2008).
11. C. Majidi, Soft Robotics: A perspective–current trends and prospects for the future. *Soft Robotics* **1**, 5–11 (2013).
12. S. Kim, C. Laschi, B. Trimmer, Soft robotics: A bioinspired evolution in robotics. *Trends Biotechnol.* **31**, 287–294 (2013).
13. D. Rus, M. T. Tolley, Design, fabrication and control of soft robots. *Nature* **521**, 467–475 (2015).
14. N. W. Pikul, S. Li, H. Bai, R. T. Hanlon, I. Cohen, R. F. Shepherd, Stretchable surfaces with programmable 3D texture morphing for synthetic camouflaging skins. *Science* **358**, 210–214 (2017).
15. A. Menciassi, D. Accoto, S. Gorini, P. Dario, Development of a biomimetic miniature robotic crawler. *Auton. Robotics* **21**, 155–163 (2006).
16. J. Z. Ge, A. A. Calderón, N. O. Pérez-Arancibia, An earthworm-inspired soft crawling robot controlled by friction. arXiv 1707.04084 (2017).
17. K. Suzumori, T. Hama, T. Kanda, New pneumatic rubber actuators to assist colonoscope insertion, in *IEEE International Conference on Robotics and Automation*, (ICRA, 2006), pp. 1824–1829.
18. R. F. Shepherd, F. Ilievski, W. Choi, S. A. Morin, A. A. Stokes, A. D. Mazzeo, X. Chen, M. Wang,G. M. Whitesides, Multigait soft robot. *Proc. Natl. Acad. Sci. U.S.A.* **108**, 20400–20403 (2011).
19. F. Connolly, P. Polygerinos, C. J. Walsh, K. Bertoldi, Mechanical programming of soft actuators by varying fiber angle. *Soft Robotics* **2**, 26–32 (2015).
20. S. Seok, C. Denizel Onal, K.-J. Cho, R. J. Wood, D. Rus, S. Kim, Meshworm: A peristaltic soft robot with antagonistic nickel titanium coil actuators. *IEEE/ASME Trans. Mechatronics* **18**, 1485–1497 (2013).
21. T. Umedachi, V. Vikas, B. A. Trimmer, Softworms: The design and control of non-pneumatic, 3D-printed, deformable robots. *Bioinspir. Biomim.* **11**, 025001 (2016).
22. H. A. Abdel-Aal, M. El Mansori, Tribological analysis of the ventral scale structure in a *Python regius* in relation to laser textured surfaces. *Surf. Topogr. Metrol. Prop.* **1**, 015001 (2013).
23. H. Marvi, Y. Han, M. Sitti, Actively controlled fibrillar friction surfaces. *Appl. Phys. Lett.* **106**, 051602 (2015).
24. S. Das, N. Cadirov, S. Chary, Y. Kaufman, J. Hogan, K. L. Turner, J. N. Israelachvili, Stick–slip friction of gecko-mimetic flaps on smooth and rough surfaces. *J. R. Soc. Interface* **12**, 20141346 (2015).
25. T. Yamaguchi, Y. Sawae, S. M. Rubinstein, Effects of loading angles on stick–slip dynamics of soft sliders. *Extreme Mech. Lett.* **9**, 331–335 (2016).
26. T. C. Shyu, P. F. Damasceno, P. M. Dodd, A. Lamoureux, L. Xu, M. Shlian, M. Shtein, S. C. Glotzer, N. A. Kotov, A kirigami approach to engineering elasticity in nanocomposites through patterned defects. *Nat. Mater.* **14**, 785–789 (2015).
27. M. K. Blees, A. W. Barnard, P. A. Rose, S. P. Roberts, K. L. McGill, P. Y. Huang, A. R. Ruyack, J. W. Kevek, B. Kobrin, D. A. Muller, P. L. McEuen, Graphene kirigami. *Nature* **524**, 204–207 (2015).
28. A. Rafsanjani, K. Bertoldi, Buckling-induced kirigami. *Phys. Rev. Lett.* **118**, 084301 (2017).
29. Y. Tang, G. Lin, S. Yang, Y. K. Yi, R. D. Kamien, J. Yin, Programmable kiri-kirigami metamaterials. *Adv. Mater.* **29**, 1604262 (2017).
30. S. Shian, K. Bertoldi, D. R. Clarke, Dielectric elastomer based "grippers" for soft robotics. *Adv. Mater.* **27**, 6814–6819 (2015).
31. T. Li, G. Li, Y. Liang, T. Cheng, J. Dai, X. Yang, B. Liu, Z. Zeng, Z. Huang, Y. Luo, T. Xie, W. Yang, Fast-moving soft electronic fish. *Sci. Adv.* **3**, e1602045 (2017).
32. A. Miriyev, K. Stack, H. Lipson, Soft material for soft actuators. *Nat. Commun.* **8**, 596 (2017).
33. H. Yuk, S. Lin, C. Ma, M. Takaffoli, N. X. Fang, X. Zhao, Hydraulic hydrogel actuators and robots optically and sonically camouflaged in water. *Nat. Commun.* **8**, 14230 (2017).
34. B. C. Jayne, S. J. Newman, M. M. Zentkovich, H. M. Berns, Why arboreal snakes should not be cylindrical: Body shape, incline and surface roughness have interactive effects on locomotion. *J. Exp. Biol.* **218**, 3978–3986 (2015).
35. F. Connolly, C. J. Walsh, K. Bertoldi, Automatic design of fiber-reinforced soft actuators for trajectory matching. *Proc. Natl. Acad. Sci. U.S.A* **114**, 51–56 (2017).
36. A. Lamoureux, K. Lee, M. Shlian, S. R. Forrest, M. Shtein, Dynamic kirigami structures for integrated solar tracking. *Nat. Commun.* **6**, 8092 (2015).
37. M Isobe, K. Okumura, Initial rigid response and softening transition of highly stretchable kirigami sheet materials. *Sci. Rep.* **6**, 24758 (2016).
38. M. Senn, C. Eberl, Digital Image Correlation and Tracking (2015); https://uk.mathworks.com/matlabcentral/fileexchange/50994-digital-imagecorrelation-and-tracking.

Acknowledgments

Funding: Research was supported by the NSF under grant number DMR-1420570. A.R. acknowledges the financial support provided by the Swiss National Science Foundation under grant number P300P2-164648. **Author contributions:** A.R. and K.B. conceived the concepts and designed the research. A.R., Y.Z., and B.L. built the crawlers and performed the experiments. B.L. developed the control unit for the untethered crawler. A.R. and S.M.R developed the theoretical model. A.R., S.M.R., and K.B. analyzed the data and wrote the paper.

K.B. supervised the research. **Competing interests:** A.R. and K.B. are named inventors on U.S. Provisional Patent Application No. 62,624,371, which has been submitted by President and Fellows of Harvard College and generally covers transformation of a 2D sheet into a 3D-patterned, perforated surface, such as a kirigami structure induced by buckling of interconnecting ligaments. The other authors declare no competing interests. **Data and materials availability:** All data needed to support the conclusions are in the main text or the Supplementary Materials.

Submitted 13 December 2017
Accepted 2 February 2018
Published 21 February 2018
10.1126/scirobotics.aar7555

Citation: A. Rafsanjani, Y. Zhang, B. Liu, S. M. Rubinstein, K. Bertoldi, Kirigami skins make a simple soft actuator crawl. *Sci. Robot.* **3**, eaar7555 (2018).

robotics.sciencemag.org/cgi/content/full/3/15/eaar7555/DC1

Science Robotics

Supplementary Materials for

Kirigami skins make a simple soft actuator crawl

Ahmad Rafsanjani, Yuerou Zhang, Bangyuan Liu, Shmuel M. Rubinstein, Katia Bertoldi*

*Corresponding author. Email: bertoldi@seas.harvard.edu

Published 21 February 2018, *Sci. Robot.* **3**, eaar7555 (2018)
DOI: 10.1126/scirobotics.aar7555

The PDF file includes:

Other Supplementary Material for this manuscript includes the following:
(available at robotics.sciencemag.org/cgi/content/full/3/15/eaar7555/DC1)

Movie S2 (.mp4 format). A fiber-reinforced extending actuator is placed over a rough surface and is subjected to cyclic inflation/deflation.
Movie S3 (.mp4 format). Assembly of a kirigami-skinned soft crawler.
Movie S4 (.mp4 format). Motion of the crawlers during six inflation cycles with $V \in [0,24]$ ml.
Movie S5 (.mp4 format). Motion of the crawlers when a total volume $V_{tot} = 120$ ml of air is supplied by cyclically inflating and deflating them between $V_{max} = 24$ ml and $V_{min} \in [0,V_{max}]$.
Movie S6 (.mp4 format). Fully untethered kirigami skinned crawlers with triangular, circular, and trapezoidal kirigami skins.
Movie S7 (.mp4 format). An untethered crawler with circular kirigami skin propels itself over asphalt.
Movie S8 (.mp4 format). An untethered crawler with trapezoidal kirigami skin climbs a concrete ramp.
Movie S9 (.mp4 format). An untethered crawler with triangular kirigami skin propels itself over rough stone.
Movie S10 (.mp4 format). Motion of an untethered crawler with trapezoidal kirigami skin for P_{min} = 1, 4, 8, and 12 kPa and P_{max} = 16 kPa.

Supplementary sections S1 to S4.

S1 Fabrication

The kirigami-skinned soft crawlers investigated in this study comprise a fiber-reinforced soft actuator with a kirigami sheet wrapped around. In this Section, we describe our methods for fabricating both the fiber-reinforced soft actuators and the kirigami sheets as well as for assembling the kirigami-skinned crawlers.

Fiber-reinforced soft actuators

The fiber-reinforced soft actuators considered in this study are made of platinum-catalyzed silicone rubber (Ecoflex 00-30, Smooth-On, Inc.) and have initial length $\tilde{L}_0$ = 164 mm and a triangular cross section with edge w = 25 mm and thickness t_a = 1.5 mm (Fig. S1D). Note that the triangular cross section resembles that of snakes, which take advantage of a triangular cross-section to increase the contact area and minimize the lateral rolling for a more efficient locomotion [34].

The actuator mold is designed in Solidworks and 3d printed using an Objet Connex 500 printer (Stratasys) (Fig. S1A). The mold is assembled and held together firmly with clamps. The inner surfaces of the mold are exposed to Universal Mold Release spray (Smooth-On, Inc.) and then the elastomer (Ecoflex 00-30, shear modulus μ_a = 30 kPa) is poured into the mold (Fig. S1B) and degassed in a vacuum chamber for a couple of minutes. A triangular prismatic rod is inserted into the mold to create the core of the actuator. The rod slots into a triangular indentation at the bottom of the mold and a cap holds the rod in place at the top of the mold (Fig. S1C). The elastomer is left overnight at room temperature to cure. The next day, the plastic mold is removed.

To maximize the elongation of the actuator upon inflation and constrain its deformation in the radial direction, the elastomeric tube is surrounded by stiff Kevlar fibers arranged in a helical pattern [35]. Since a pure extending actuator requires a fiber angle of 0°, but such

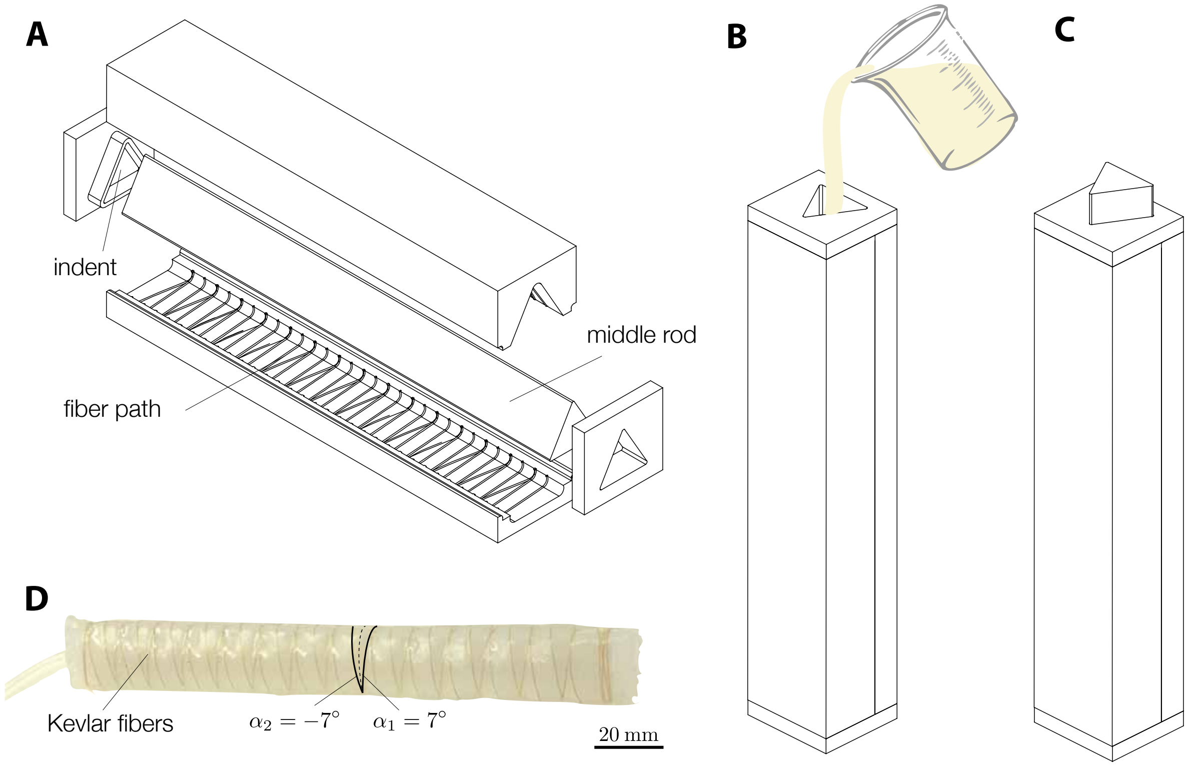

Figure S1. **Fabrication of an extending fiber-reinforced actuator.** (**A**) Exploded view of the 3D printed mold showing the indent in the rear cap and the path for fibers. (**B**) The elastomer is poured into the mold. (**C**) The rod is inserted into the mold and held in place by the caps. (**D**) Picture of the fabricated fiber-reinforced actuator.

angle is difficult to achieve in practice, we use two families of fibers arranged symmetrically at a characteristic angle $\alpha_1 \simeq 7^\circ$ and $\alpha_2 \simeq -7^\circ$ (Fig. S1D). This leads to an actuator that purely extend and does not twist and expand. To control the fiber angle during fabrication, ridges are introduced on the surface of the mold. These leave grooves on the actuator, which define the path for winding the fibers. At each end of the actuator the fiber is looped around a few times and tied. The fibers and knots are held in place by brushing the surface of the actuator with a very thin layer of uncured elastomer. The actuator is then carefully removed from the rod. The ends of the actuator are plugged with Sil-Poxy, and a vented screw is inserted at one end. The Sil-Poxy is allowed to cure for 24 hours.

Kirigami sheets

The kirigami sheets are fabricated by laser cutting an array of 9×32 cuts into polyester plastic sheets (Artus Corporation, NJ) with Youngs modulus $E = 4.33$ GPa and Poissons ratio $\nu = 0.4$.

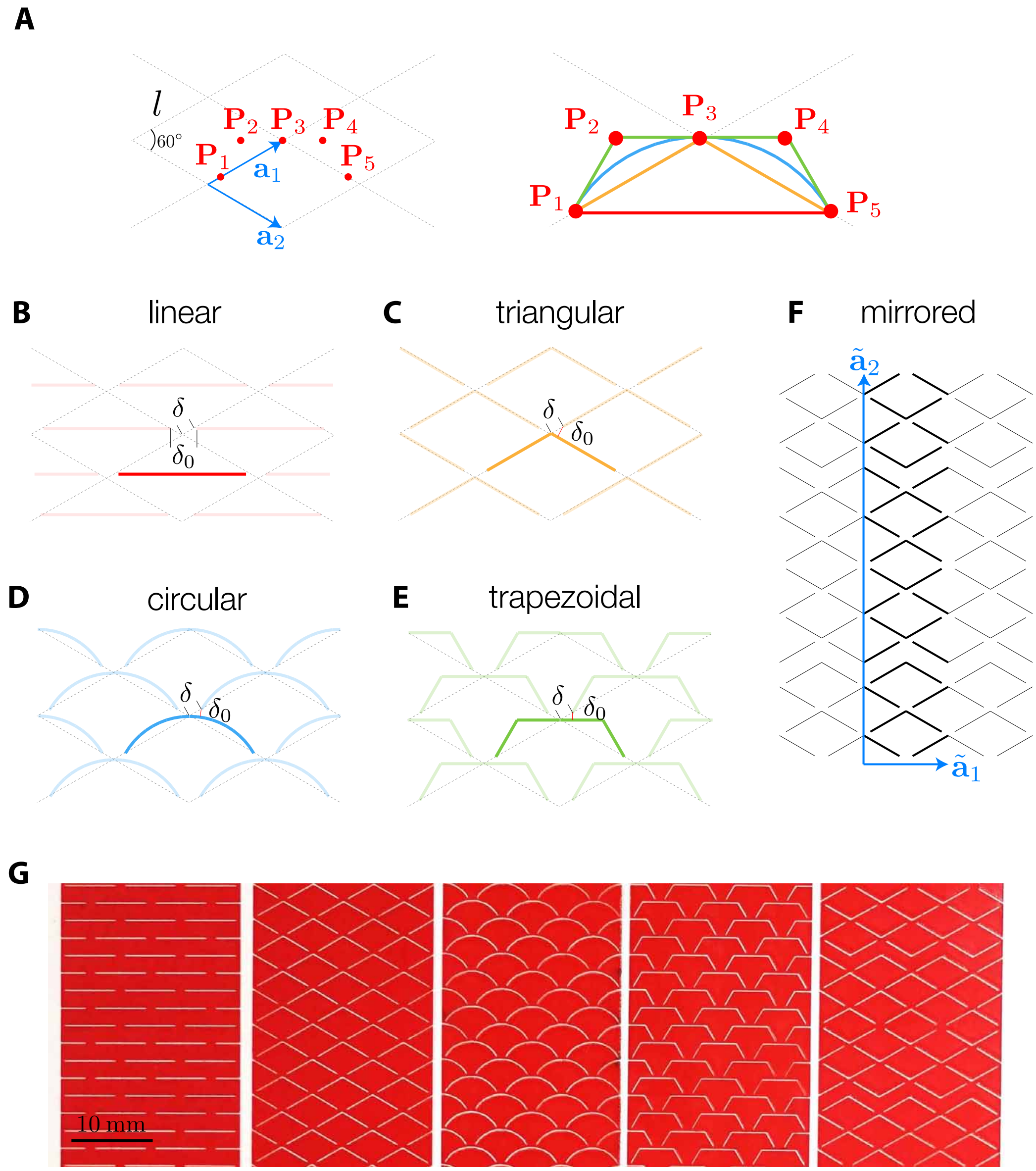

Figure S2. Kirigami patterns. (**A**) Unit cell and points used to generate different cut shapes. (**B**)-(**E**) Four different cut shapes are considered in this study: (**B**) linear cuts, (**C**) triangular cuts, (**D**) circular cuts and (**E**) trapezoidal cuts. (**F**) We also consider a mirrored pattern based on triangular cuts.The repeating units are highlighted in each graph. (**G**) Kirigami skeets fabricated by laser cutting a polyester plastic sheet.

In all our designs the cuts are arranged on a triangular lattice with unit cell defined by the primitive vectors $\mathbf{a}_1 = [l \cos \pi/6, \; l \sin \pi/6]$ and $\mathbf{a}_2 = [l \cos \pi/6, \; -l \sin \pi/6]$ (Fig. S2A). Each unit cell comprises a cut with end points $\mathbf{P}_1 = \mathbf{a}_1 \delta/l$ and $\mathbf{P}_5 = \mathbf{a}_1 + \mathbf{a}_2(1 - \delta/l)$ (Fig. S2A). In this study we consider four different cut shapes:

- *Linear cuts:* these consists of horizontal straight cuts that connect the points $\mathbf{P}_1$ and $\mathbf{P}_5$ and define an array of hinges with minimum width $\delta_0 = 2\delta \cos \pi/6$ (Fig. S2B). Note that the response of kirigami sheets with such perforation pattern has been investigated in several studies [30, 31, 36, 37].
- *Triangular cuts:* these consists of two straight cuts connecting the points $\mathbf{P}_1$, $\mathbf{P}_3 = \mathbf{a}_1$ and $\mathbf{P}_5$ and define an array of hinges with minimum width $\delta_0 = \delta \cos \pi/6$ (Fig. S2C).
- *Circular cuts:* these consists of circular segments with end points $\mathbf{P}_1$ and $\mathbf{P}_5$ and radius $r = l - \delta$ and define an array of hinges with minimum width $\delta_0 = \sqrt{l^2 + \delta^2 - l\delta} - (1 - \delta)$ (Fig. S2D).
- *Trapezoidal cuts:* these consists of three straight cuts connecting the points $\mathbf{P}_1$, $\mathbf{P}_2 = \mathbf{a}_1 - [(l - \delta) \tan \pi/6, 0]$, $\mathbf{P}_4 = \mathbf{a}_1 + [(l - \delta) \tan \pi/6, 0]$ and $\mathbf{P}_5$ and define an array of hinges with minimum width $\delta_0 = \delta \sin \pi/6$ (Figure S2E).

All fabricated kirigami sheets are characterized by $\delta/l = 0.156$, with $l = 4.5$ mm.

Finally, to investigate the effect of the asymmetry of the kirigami patterns on the motion of the crawlers, we also consider a mirrored triangular pattern comprising triangular cuts that point both upward and downward (Fig. S2F). The repeating unit of the mirrored design is defined by the primitive vectors $\tilde{\mathbf{a}}_1 = [2l\cos \pi/6, 0]$ and $\tilde{\mathbf{a}}_2 = [0, 16l\sin \pi/6]$.

Assembly of the kirigami-skinned crawlers

To assemble the kirigami-skinned crawlers, we wrap the kirigami sheet around the fiber-reinforced actuator. To this end, we use a double-sided adhesive sheet with a thickness of 0.07 mm (23205-1009, Blick Art Materials, IL). More specifically,

- *Step 1*: we start by cutting and removing from the adhesive sheet the area occupied by the kirigami sheet (a rectangle of 74 mm$\times$ 164 mm) connected to the two triangular caps (Fig. S3A). We also introduce into the adhesive one layer of the kirigami cuts along one of the long edges of the removed rectangular area (this area is then used to bond the two edges together and wrap the sheet around the actuator - see Step 4).

- *Step 2*: we remove the top cover of the adhesive layer and attach the plastic sheet (Artus Corporation, NJ) to it. We introduce the kirigami pattern in the area of the plastic sheet from which the adhesive has been removed (Fig. S3B). Moreover, to facilitate assembly of the kirigami-skinned crawler, fold lines are precisely raster engraved (see red lines in Fig. S3B-top) and a circular opening is introduced in the rear cap for the inlet tube to pass through.

- *Step 3*: slits are introduced through both layers along the boundaries of the kirigami skin, leaving flaps to facilitate the assembly. The kirigami skin is removed from the layered sheet (Fig. S3C).

- *Step 4*: the kirigami-skinned crawlers is assembled (Fig. S3D). First, we pass the inlet tube through the circular opening in the rear cap of the kirigami skin. Then, we bond the ends of the kirigami skin together by overlapping the double-sided adhesive flaps. Note that no glue is used in this step, but only the double-sided tape already incorporated into the part. The assembled kirigami-skinned soft crawlers has an array of 3×32 cuts on each of its three faces.

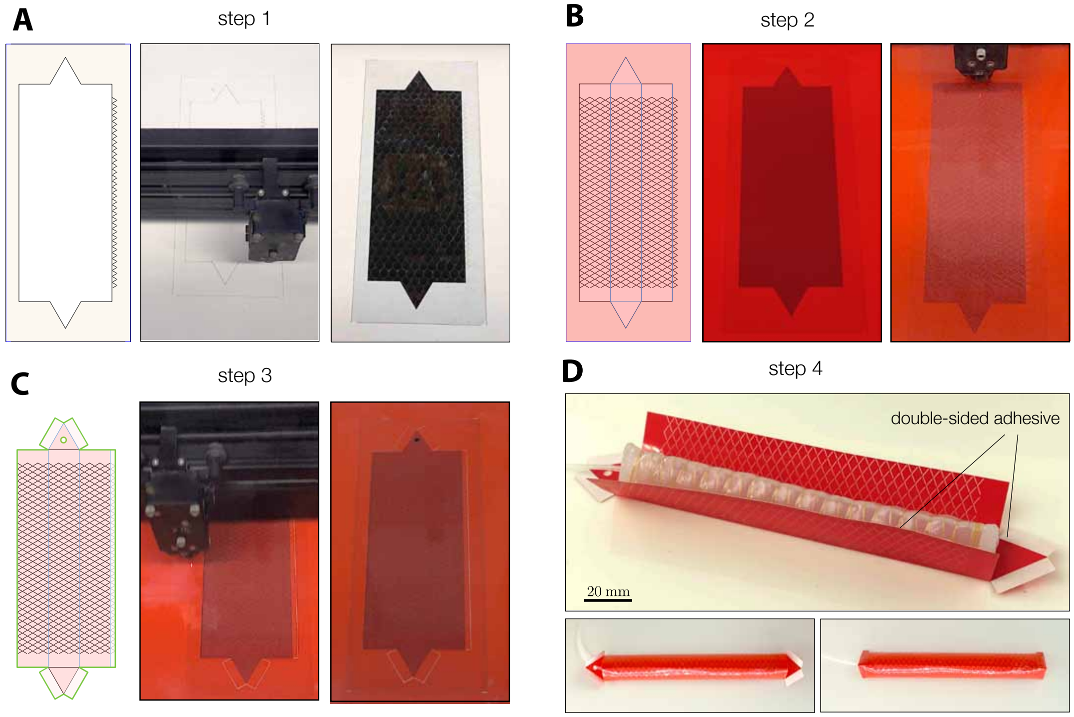

Figure S3. Fabrication and assembly of kirigami-skinned crawlers. (**A**) Step 1, cutting the adhesive sheet. (**B**) Step 2, attaching and cutting plastic shim. (**C**) Step 3, cutting the boundaries. (**D**) Step 4, covering the soft actuator with the kirigami skin. First, we pass the inlet tube through the circular opening in the rear cap of the kirigami skin. Then, we bond the ends of the kirigami skin together by overlapping the double-sided adhesive flaps.

Assembly of untethered kirigami-skinned crawlers

The crawlers described in the previous Section are actuated pneumatically using air transferred to them from a stationary source via a flexible tube. However, real-world applications require systems that are capable of operating without the constraint of a tether. As a first step in this direction, we also build a fully untethered kirigami-skinned soft crawler by integrating on-board control, sensing, actuation and power supply (Fig. S5). Specifically,

- *Control and Sensing:* the control comprises both on-board and off-board systems, which communicate with each other using the 2.4GHz ZigBee communication protocol via a wireless serial transceiver module (model CC2530 - WeBee IOT Technology Co., Ltd.). The on-board system consists of a micro-controller unit (model ATMega328, Arduino Nano). In order to build a feedback control system, we use a pressure sensor (model XGZP6847 - CFSensor) on-board to detect the real-time pressure of the elastomeric actuator and send this information to the off-board system as the feedback signal. Based on the received pressure values, a simple on-off control algorithm implemented in MATLAB determine the open/closed states of the two valves responsible for inflation and deflation of the soft actuator. When the measured pressure is lower than a prescribed minimum pressure P_{min}, the controller sets the status of the inflation valve to *open* and that of the deflation one to *closed*. Differently, when the measured pressure is higher than a prescribed maximum pressure P_{max}, the controller sets the status of the inflation valve to *closed* and that of the deflation one to *open*.

- *Actuation:* The crawler is actuated using a micro pneumatic diaphragm pump (model SC3101PM - Shenzhen Skoocom Electronic Co., Ltd.) and two two-three-way miniature pneumatic solenoid valves (X-Valve, Parker Co.). The power of pump can be controlled from zero to its maximum by the micro-controller unit with the help of a motor controller (model TB6612FNG - KNACRO). Note that the pump has a maximum power of 0.347W, which is achieved when the input voltage of the system is 7.4V.

- *Power supply:* The on-board system is powered by two micro 3.7V lithium battery (model LP401230 - Shenzhen PKCell Battery Co., Ltd.) to provide 7.4V. The pump is powered by 7.4V, while the micro-controller unit, the pressure sensor and both valves are powered by 5V converted from 7.4V via a voltage regulator (model LM7805 - Fairchild Semiconductor).

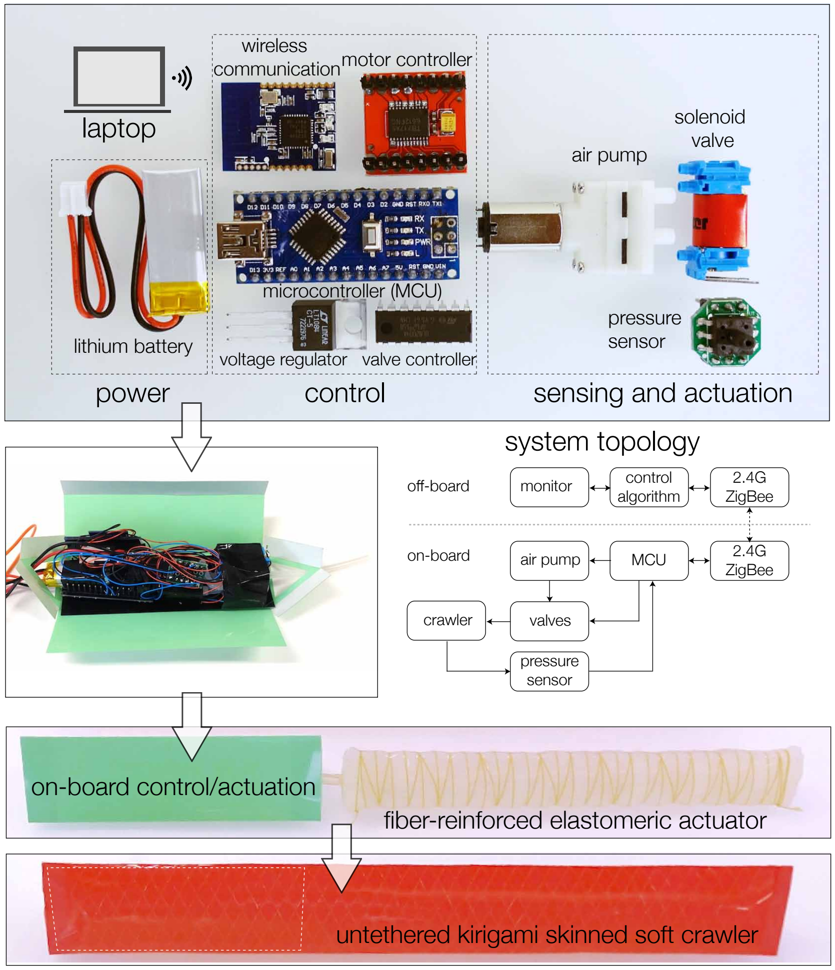

Figure S4. Untethered kirigami-skinned crawler. Components of our untethered kirigami-skinned soft crawler with on-board control, actuation and sensing.

It is important to note that all the on-board components have a total weight of 45g and can be packed into a triangular prism with length of 10 cm and sides of 3cm (Fig. S5). Such small volume is then attached to the back of a fiber-reinforced soft actuator and both parts are covered by a kirigami skin to form a fully untethered kirigami-skinned soft crawler.

S2 Testing

In this Section we first describe the mechanical tests that we use to characterize the response of the fiber-reinforced soft actuators and kirigami sheets separately. We then provide details on the mechanical tests conducted to characterize the behavior of the assembled kirigami-skinned crawlers.

Fiber-reinforced soft actuators

The fiber-reinforced soft actuators considered in this study are tested using a syringe pump (Standard Infuse/Withdraw PHD Ultra; Harvard Apparatus) equipped with two 50 mL syringes that have an accuracy of 0.1% (1000 series, Hamilton Company). The experiments are conducted under volume control at a rate of 300 mL/min and the maximum supplied volume of air is V_{max} = 24 mL. During inflation the pressure P is measured using a silicon pressure sensor (MPX5100; Freescale Semiconductor) with a range of 0-100 kPa and an accuracy of ±2.5%, which is connected to a data acquisition system (NI USB-6009, National Instruments). The elongation of the actuators is monitored by putting two markers on both ends of each actuator, and recording their position with a high-resolution camera (SONY RX100V). The axial strain experienced by the actuator is then calculated as

$$\varepsilon = \frac{\tilde{L} - \tilde{L}_0}{\tilde{L}_0}, \tag{S1}$$

where $\tilde{L}$ and $\tilde{L}_0$ denote the deformed (i.e. in the inflated state) and undeformed (i.e. prior to inflation) length of the actuator, respectively. Each experiment is repeated 5 times and the final response of the actuator shown in Fig. S5A-B is determined by averaging the results.

In Fig. S5A we report the evolution of the axial strain ε as a function of the supplied volume V (normalized by V_{max}). The results confirm that our actuators significantly extend upon inflation, with ε = 0.25 at $V = V_{max}$ = 24 ml. In Fig. S5B we then show the

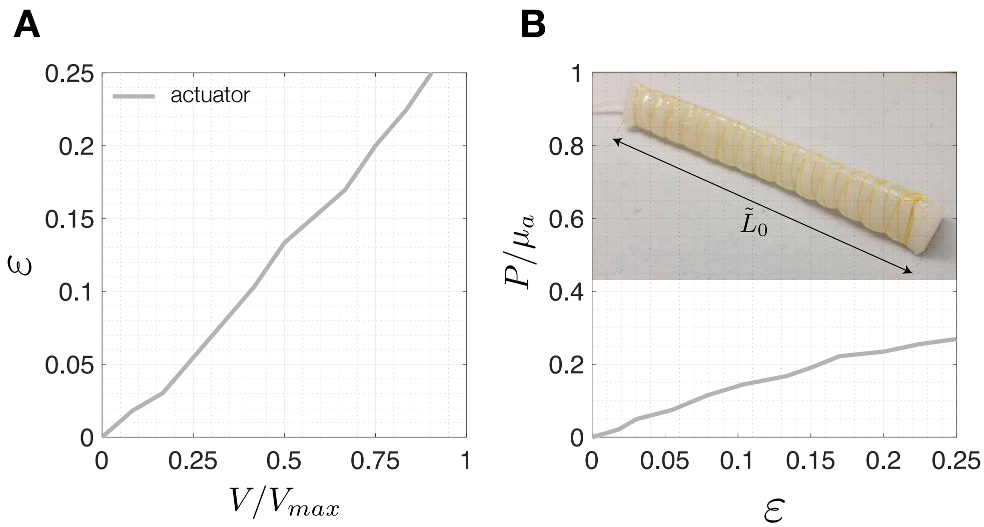

Figure S5. **Mechanical response of the actuator.** (**A**) Axial strain *ε* versus supplied volume *V* (normalized by V_{max} = 24 ml) for the fiber-reinforced actuator. (**B**) Internal pressure of the actuator (normalized by μ_a = 30 kPa) as a function of its elongation.

evolution of the pressure *P* (normalized by the shear modulus of the elastomeric material used to fabricate the actuator, μ_a) as a function of the axial strain *ε*.

Kirigami sheets

The quasi-static uniaxial tensile response of the kirigami sheets is probed by stretching flat samples with 3 × 32 cuts. To this end, we use an uniaxial testing machine (Instron 5566) equipped with a 100N load cell. All tests are conducted under displacement control at a rate of mm/s and continued until failure.

In Fig. S6A we report the experimental stress-strain responses for the five kirigami patterns considered in this study. The nominal stress of kirigami sheets s_k is normalized with the elastic Young's modulus of the plastic sheet E_s = 4.33GPa. As observed for thin sheets perforated with linear cuts [30, 37] and more recently for thin sheets with a square array of mutually orthogonal cuts [32], the response of all samples is characterized by three distinct regions: a linear elastic regime, a stress plateau following thereafter and stiffening by further extension.

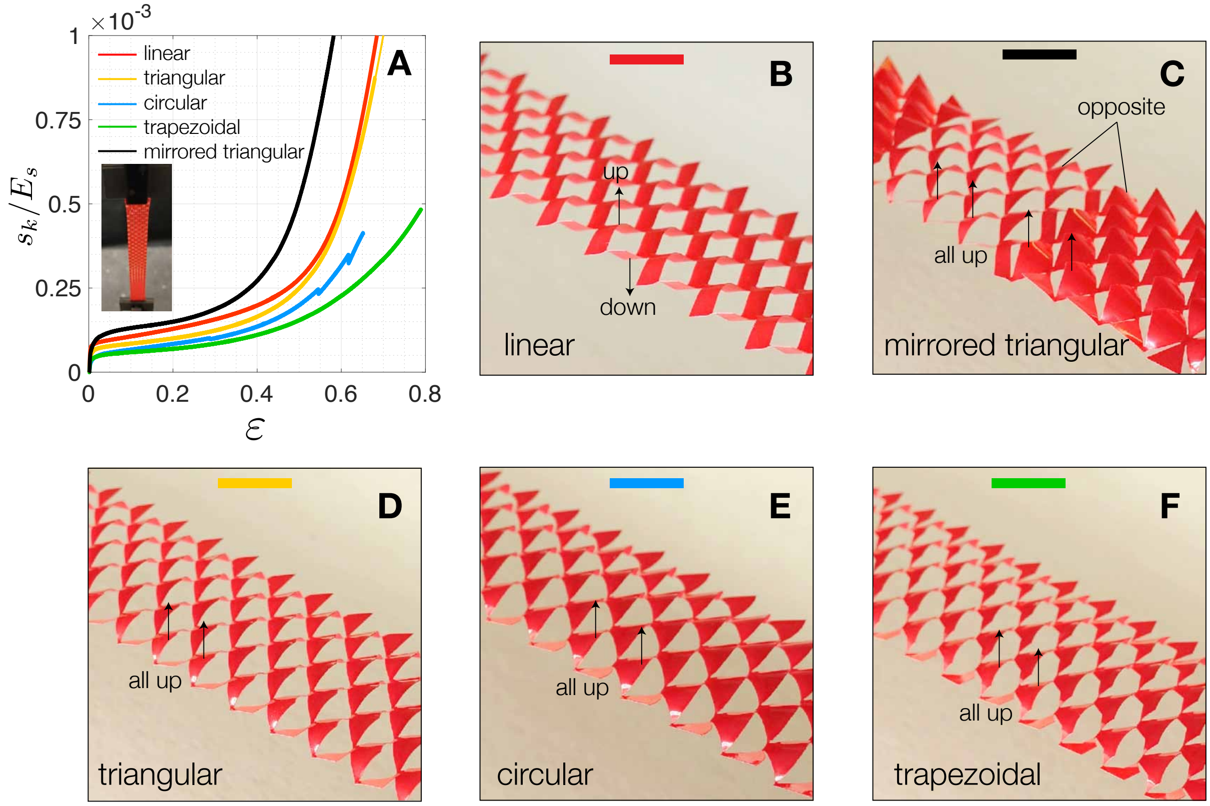

Figure S6. **Mechanical response of kirigami sheets.** (**A**) Nominal stress s_k of planar kirigami sheets (comprising 3 × 32 unit cells) normalized by the Young's modulus of the plastic sheets (E_s = 4.33GPa) versus applied strain. (**B-F**) Closeup views of 3D pop-up configurations of planar kirigami sheets with linear, mirrored triangular, triangular, circular and trapezoidal patterns at $\varepsilon = 0.2$.

While in the initial linear regime all hinges bend in-plane and the samples remain flat, the sudden departure from linearity to a plateau stress is caused by the out-of-plane buckling of the hinges, which induces the formation of 3D patterns (see Fig. S6B-F). It is important to note that, while in the sheets with linear cuts the mechanical instability results in a symmetric pattern with features moving out to both sides of the sheet, the 3D patterns induced by buckling in all other sheets are asymmetric, with features popping out only on one side of the sheet.

Finally, for large enough values of the applied strain ε the deformation mechanism of the hinges switches from bending dominated to stretching dominated. At this stage, the stress rises sharply and localized zones of intense strain (of plastic nature) develop in the hinges.

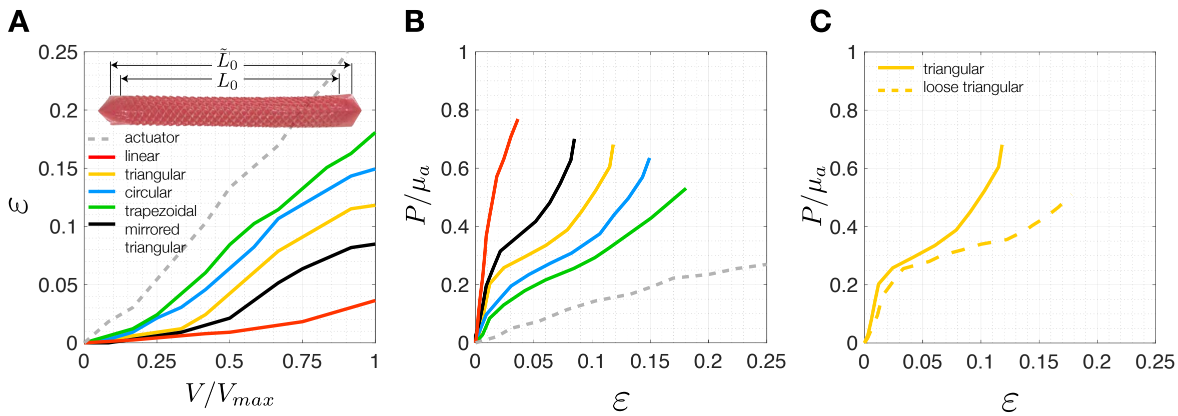

Figure S7. Mechanical response of kirigami-skinned crawlers. (**A**) Axial strain ε versus supplied volume V for the kirigami-skinned crawlers. Inset shows definition of L_0 and $\tilde{L}_0$. (**B**) Internal pressure P versus axial strain ε for the kirigami-skinned crawler. (**C**) Internal pressure P versus axial strain ε for the crawlers with a kirigami skin comprising an array with dimension reported in Section S1 (solid line) and a looser skin with all dimensions increased by 10% (dashed linev).

Kirigami-skinned crawlers

Three different set of tests are conducted to characterize the mechanical response of the assembled kirigami-skinned crawlers: one set to characterize their elongation and pressure as a function of the supplied volume, another set to investigate how inflation affects the frictional force when they move on a substrate and a final set to characterize their locomotion.

Elongation and pressure

The evolution of the elongation and pressure of our kirigami-skinned crawlers upon inflation is characterized with an experimental procedure identical to that used for the fiber-reinforced soft actuators. However, it is important to note that for the kirigami-skinned crawlers the axial strain ε is calculated using the length of the perforated part of the skin,

$$\varepsilon = \frac{L - L_0}{L_0}, \tag{S2}$$

where L_0 and L denote the undeformed and deformed lengths of the perforated part of the skin (see inset in Fig. S7A). In Fig. S7A and S7B we report the experimental results obtained for the actuators covered with the five different kirigami skins considered in this study and for comparison, we also include the results of the fiber-reinforced actuator (dashed gray line). First, we find that kirigami skins comprising an array of triangular, circular, trapezoidal and mirrored triangular cuts only moderately limit the extensibility of the soft actuator. By contrast, when a kirigami sheet with linear cuts is wrapped around the actuator, the extensibility of the resulting crawler is almost completely suppressed. This is because the symmetric out-of-plane buckling mode of the sheet with linear cuts is prevented by the presence of the actuator (see Fig. S8). As such, no mechanical instability is triggered in the kirigami sheet with linear cuts upon inflation, resulting in linear and very stiff response (see red line in Fig. S7A)

Second, Fig. S7B reveals that, with the exception of the kirigami-skinned crawler with linear cuts, all other crawlers are characterized by a pressure-elongation evolution qualitatively identical to the stress-strain curves shown in Fig. S6A (i.e. characterized by a initial linear regime, a pressure plateau and final stiffening). However, in the kirigami-skinned crawlers the transition between the plateau and the stiffening regimes occurs at much lower values of axial strain compared to the corresponding kirigami sheets. To understand the reason behind this difference, we fabricate and test an additional kirigami-skinned crawler covered by a looser skin with triangu- lar cuts. More specifically, in this looser skin all dimensions are increased by 10% compared to those described in Section S1. The results reported in Fig. S7C show that the transition between the plateau and the stiffening regimes is postponed in the actuator with the looser skin (i.e. it occurs at $\varepsilon \sim 0.15$ instead of at $\varepsilon \sim 0.08$). This indicates that the start of the stiffening regime in the kirigami soft-crawler is not due to the stretching of the hinges (as for the kirigami sheets), but to the interaction between the skin and the actuator. Upon inflation, because of both the bulging of the actuator and the positive Poisson's ratio of the kirigami sheets (which results in shrinkage of their cross-section), the kirigami sheet and the actuator get in contact. At that point the actuator starts pushing the skin, limiting its out-of-plane deformation and increasing its axial stiffness.

Finally, in Fig. S8 we report snapshots showing the evolution of the surface morphology as a function of the supplied volume for the kirigami-skinned crawlers considered in this study.

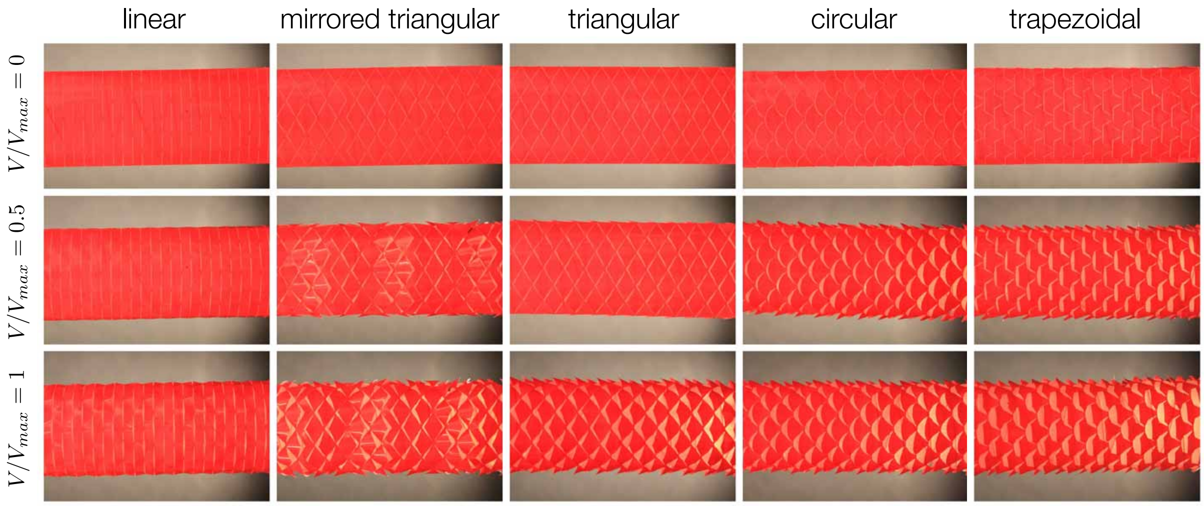

Figure S8. Evolution of surface morphology for our kirigami-skinned crawlers. Closeup views of our kirigami-skinned crawlers at different inflation levels.

Friction force

We conduct a set of tests to measure how inflation affects the frictional force when the crawlers move on a substrate. Specifically, in these experiments the crawlers are placed on a rough surface (polyurethane foam) and pushed (i.e. moved in forward direction) and pulled (i.e. moved in backward direction) for 10 mm at a constant rate of 1 mm/s using a motorized translation stage (MTS50-Z8 - Thorlabs). The resistive force in the direction of the motion (i.e. the friction force), F_{fr}, is measured using a 1 lb Load Cell (LSB200 Miniature S-Beam Load Cell, FUTEK Advanced Sensor Technology, Inc.) (see Fig. S9). We consider both the fiber-reinforced soft actuator (without kirigami skin) and kirigami-skinned crawlers with linear, triangular, circular, trapezoidal and mirrored triangular patterns. In all our tests the crawlers are pushed and pulled 5 times for different values of supplied volume (i.e. $V = 0, 6, 12, 18, 24$ mL), the last 3 of which are analyzed to characterize frictional properties of crawlers

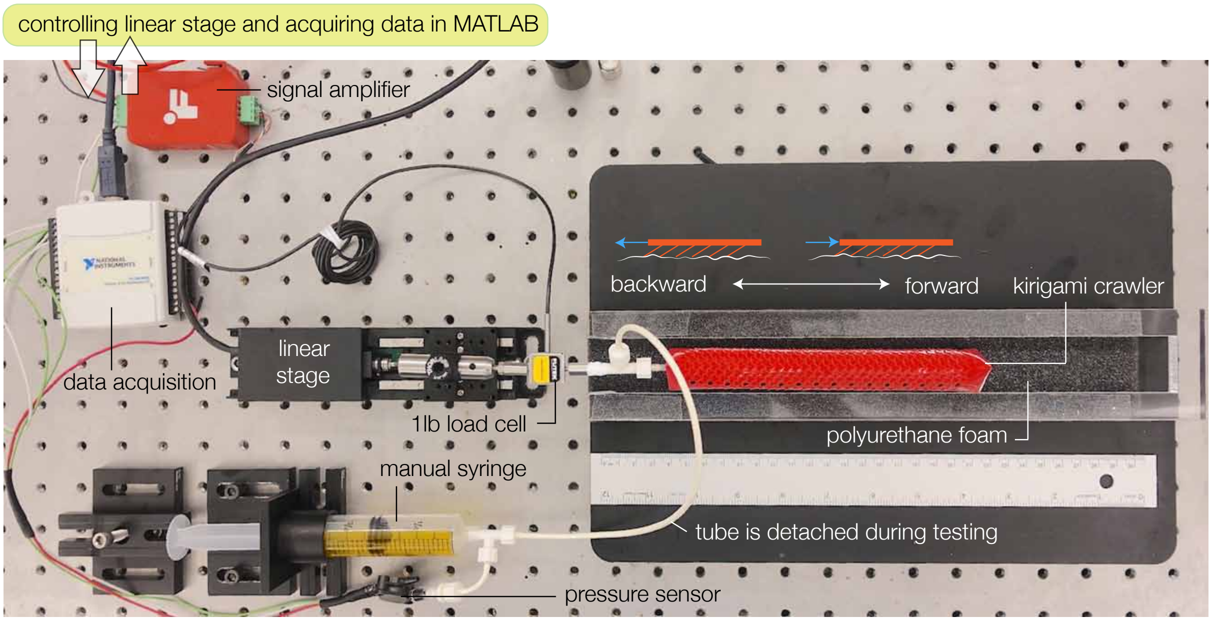

Figure S9. Friction measurement setup. Component of the experimental setup to measure the frictional prop- erties of our kirigami-skinned soft crawlers.

(since the measurements taken during the first two cycles are highly affected by the initial engagement of the sample with the substrate).

In Fig. S10 we show the acquired friction forces during the 4th cycle for different values of supplied volume (i.e. for V/V_{max} = 0, 0.25, 0.5, 0.75, 1). Our results indicate that

- the fiber reinforced actuator (without kirigami skin) and the kirigami-skinned crawler with linear cuts (i.e. the systems that do not experience buckling-induced pop-up process upon inflations) slide smoothly in both directions for all values of V. Moreover, for these systems the frictional forces recorded during pulling and pushing reach similar values, which are not affected by V.

- the kirigami-skinned crawler with triangular, circular and trapezoidal cuts (i.e. the systems that experience buckling-induced pop-up of highly directional features upon inflations) slide smoothly in both directions before the instability (i.e. for V/V_{max}

$\leq$ 0.25). Differently, for V/V_{max} > 0.25 the buckling-induced popping-out of the features defined by the cuts leads to a jerking motion in backward direction, with the crawlers that alter- natively stick to the substrate and slide over it. Such stick-slip regime is also apparent from the measured frictional force which presents a discrete sequence of sharp drops. On the other hand, the friction force is almost constant and the crawler slides smoothly when pushed in the forward direction (i.e. for $10s < t < 20s$). Finally, we also note that the instability-induced pop-up process results in a significant increase of the magnitude of F_{fr} measured during pulling.

- the kirigami-skinned crawler with mirrored triangular cuts (i.e. the system that experience buckling-induced pop-up of symmetric features upon inflations) slides smoothly in both directions before the instability. Since the mirrored pattern is inherently stiffer than the triangular one larger volumes should be supplied to trigger the instability and initiate the pop-up (i.e. $V/V_{max} \sim 0.5$). For $V/V_{max} > 0.5$ the buckling-induced popping-out of the features defined by the cuts leads to a jerking motion in both backward and forward direction and a significant increase of the magnitude of F_{fr} measured during both pulling and pushing.

An effective coefficient of friction in backward (μ_b) and forward (μ_f) directions is then extracted from our force measurements as

$$\mu_b = \frac{\left\langle F_b^{peak} \right\rangle}{F_N}, u_f = \frac{\left\langle F_f^{peak} \right\rangle}{F_N}, \tag{S3}$$

where $F_N \simeq 0.2$ N is the crawler's weight, $\langle\cdot\rangle$ denotes the mean value and F_b^{peak} and F_f^{peak} are the local peaks of Ffr recorded during pulling and pushing, respectively. Note that these peaks are calculated using the MATLAB `findpeaks` function with `MinPeakProminence` = max(F_{fr}) and `MinPeakHeight` = 0.5 max(F_{fr}).

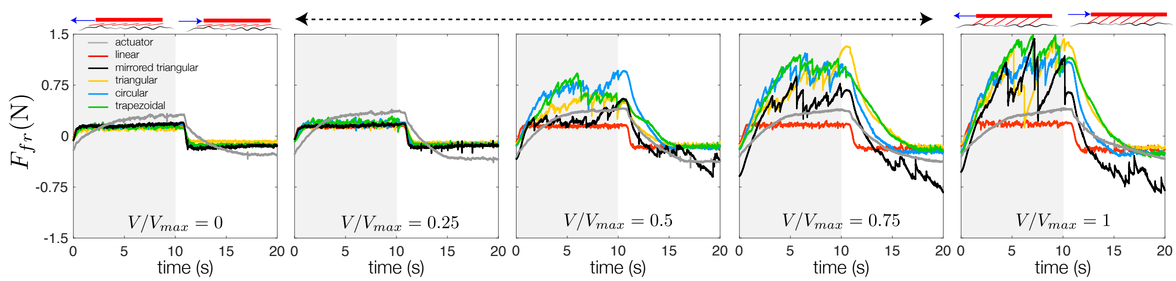

Figure S10. Friction measurements. Evolution of the friction force during the 4th pulling and pushing cycle for different values of V.

In Fig. S11 we report the experimental results obtained for the fiber-reinforced actuator (without kirigami skin) and the kirigami-skinned crawlers with linear, triangular, circular, trapezoidal and mirrored triangular patterns. We find that

- for the fiber-reinforced actuator (Fig. S11A) and the kirigami-skinned crawlers with linear cuts (Fig. S11B) the coefficients of friction in forward and backward directions are almost identical and not affected by V (i.e. $\mu_f \simeq \mu_b \simeq$ constant).

- for the kirigami-skinned crawlers with triangular (Fig. S11D), circular (Fig. S11E) and trapezoidal (Fig. S11F) cuts, $\mu_b \simeq \mu_f$ if $V/V_{max} < 0.25$, but $\mu_b >> \mu_f$ if $V/V_{max} > 0.25$.

- for the kirigami-skinned crawler with mirrored triangular cuts μ_f and μ_b start to increase for $V/V_{max} > 0.5$ and remain of comparable magnitude (i.e. $\mu_f \sim \mu_b$) (Fig. S11C)

Finally, we also test a crawler with a plastically deformed kirigami skin. Specifically, we consider a kirigami skin with triangular cuts and, before wrapping it around the actuators, we largely stretch it, so that in the post-buckling regime plastic strains develop in the ligament between the cuts, creating a permanent pop-up pattern. The results reported in Fig. S12A indicate that for all considered values of V this crawler slides smoothly when pushed in the forward direction but sticks to the substrate and slides over it when pulled it in the backward direction (such stick-slip regime is also apparent from the measured frictional force which presents a discrete sequence of sharp drops). As such, the crawler with plastically deformed

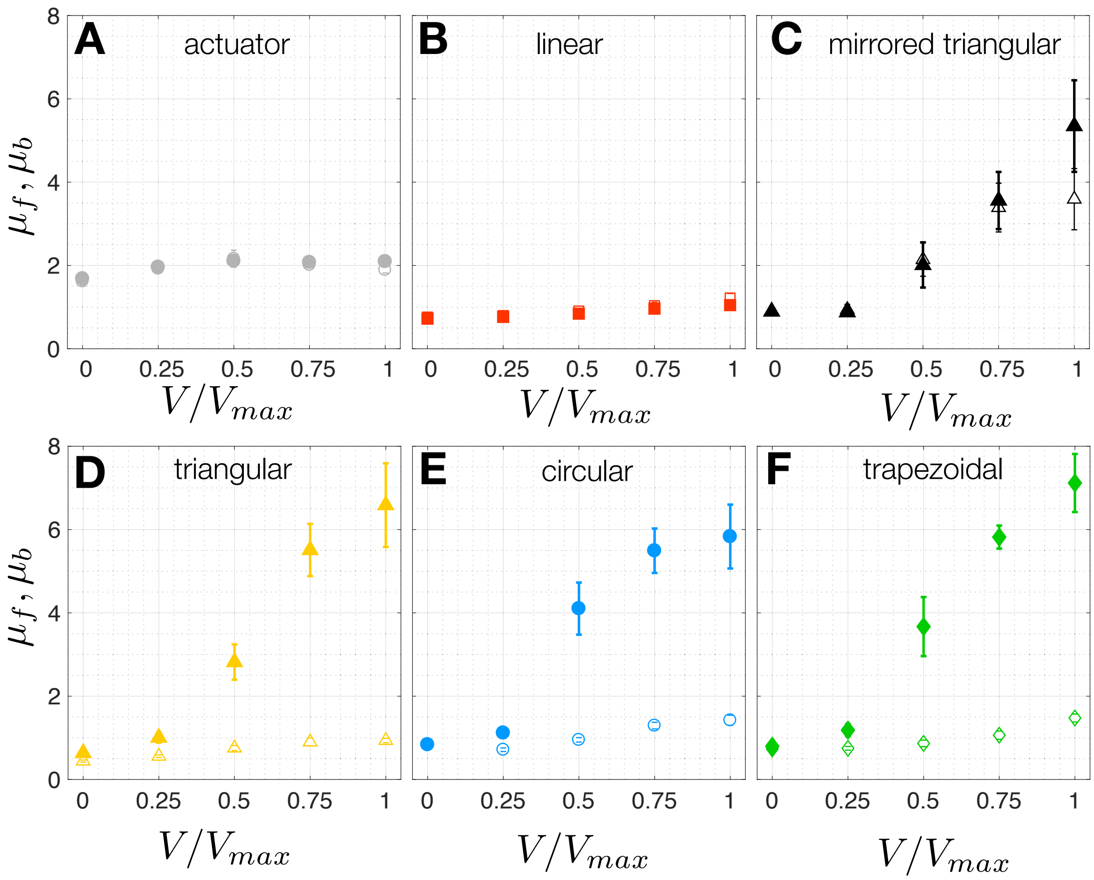

Figure S11. Effective friction coefficients. Effective friction coefficients for (**A**) the fiber-reinforced soft ac- tuator and kirigami-skinned crawlers with (**B**) linear, (**C**) mirrored triangular, (**D**) triangular, (**E**) circular and (**F**) trapezoidal cuts.

kirigami skin exhibits highly anisotropic frictional properties through the entire actuation process (Fig. S12B).

Locomotion

To characterize the ability of our kirigami-skinned crawler to move we place them on a rough surface (polyurethane foam) and repeatedly inflate them by supplying 24 mL of air and deflate them by extracting the same amount of fluid. During these tests we record the motion of the crawlers using a high-resolution camera (SONY RX100V) at a frame rate of 30 fps and determine their displacement using an open-source digital image correlation and tracking

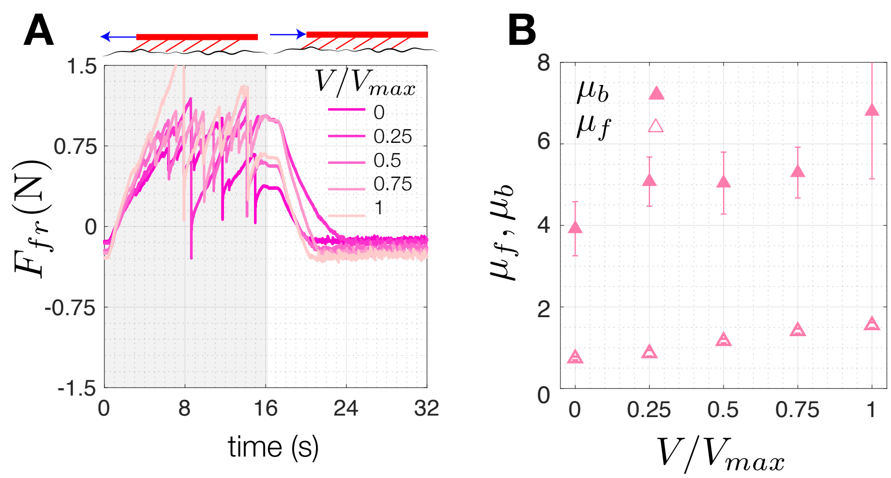

Figure S12. Frictional properties of a crawler with a plastically deformed skin. (**A**) Evolution of the friction force during the 4th pulling and pushing cycle for different values of V . (**B**) Effective friction coefficients in forward and backward direction for the plastically deformed kirigami-skinned crawlers.

package [38]. Specifically, we track the position of 16 markers uniformly placed on the skin of the crawlers and use these data to characterize displacement, velocity and location of the anchor point.

While in Fig. 3 of the main text we present results for the tethered crawlers that are actuated pneumatically using air transferred to them from a stationary source via a flexible tube, we also characterize the ability to move of an untethered kirigami-skinned crawler with trapezoidal cuts. In this case the tests are conducted under pressure control conditions, the maximum pressure is set to P_{max} = 16 kPa and the minimum pressure is varied (i.e P_{min} = 1 kPa, 4 kPa, 8 kPa and 12 kPa) and we use the on-board pressure sensor to switch between inflation and deflation. In Fig. S13A we report the pressure signal detected by the on-board pressure sensor in our experiments, while in Fig. S13B we show the corresponding displacement of the center of the crawler. Similarly to the case of the corresponding tethered crawler, also here we find that the locomotion efficiency of the crawlers can be improved by carefully choosing the minimum pressure. Specifically, we find that the tested crawler with P_{min} = 1 kPa, 4 kPa, 8 kPa and

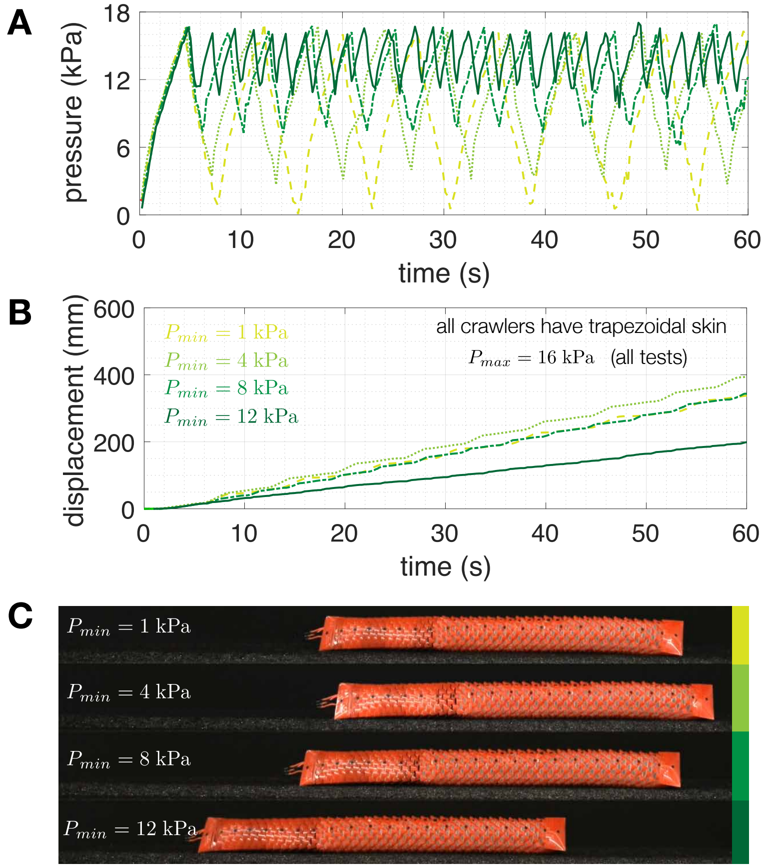

Figure S13. Locomotion of our untethered kirigami-skinned crawler. (**A**) Evolution of pressure as a function of time. (**B**) Evolution of displacement as a function of time. (**C**) Snapshots of the crawlers at the end of our experiments (i.e. after 60 seconds).

12 kPa advance by u = 338 mm, 394 mm, 344 mm and 199 mm per minute, respectively, indicating that P_{min} = 4 kPa is optimal for this specific crawler. Finally, snapshots of the crawler at the end of our experiments (i.e. after 60 seconds) are shown in Fig. S13C.

S3 Analytical Models

In this Section we present our analytical efforts to predict the locomotion efficiency of our kirigami-skinned soft crawlers. Such models, although simplified, help us getting a deeper understanding of their response.

Relation between the location of the anchor point and the measured effective friction coefficients

To connect the measured effective coefficients of friction (μ_f and μ_b) of our kirigami-skinned crawlers to the location of their anchor point (x_a), we neglect inertial forces (due to slow nature of the crawling motion) and impose static equilibrium in the direction of motion by balancing the friction forces acting on the two sides of the crawlers' instantaneous anchor point (see Fig. S14). Assuming that the mass of crawlers is uniformly distributed along their length with a linear density $\rho = m/L$, we find that during inflation

$$\int_{-\frac{1}{2}L}^{x_a} \rho g \mu_b dx - \int_{x_a}^{\frac{1}{2}L} \rho g \mu_f dx = 0, \tag{S4}$$

while during deflation

$$-\int_{-\frac{1}{2}L}^{x_a} \rho g \mu_f dx + \int_{x_a}^{\frac{1}{2}L} \rho g \mu_b dx = 0, \tag{S5}$$

where x_a denote the position of the anchor point measured from the center of mass. By solving Eqs. (S4) and (S5) we find that

$$\left(\frac{x_a}{L}\right)_{\text{inflation}} = -\frac{1}{2}\left(\frac{\mu_b - \mu_f}{\mu_b + \mu_f}\right), \left(\frac{x_a}{L}\right)_{\text{deflation}} = \frac{1}{2}\left(\frac{\mu_b - \mu_f}{\mu_b + \mu_f}\right), \tag{S6}$$

which provide explicit relations between the position of the anchor point and the frictional properties of the kirigami skin. Eqs. (S6) clearly indicate that, to maximize the distance traveled by the crawlers, the ratio μ_b/μ_f should be as large as possible. In such case, $x_a/L \rightarrow \pm 0.5$ and anchoring occurs at the tail during inflation/elongation and at the head during deflation/shortening, completely preventing backward sliding. Moreover, Eqs. (S6) also show that for $\mu_b \sim \mu_f$ the anchor point is located at the center of mass of the crawlers (i.e. $x_a/L \sim 0$). In such case the head and tail of the crawlers move by the same amount (but in opposite directions) during inflation and deflation and there is no advancement.

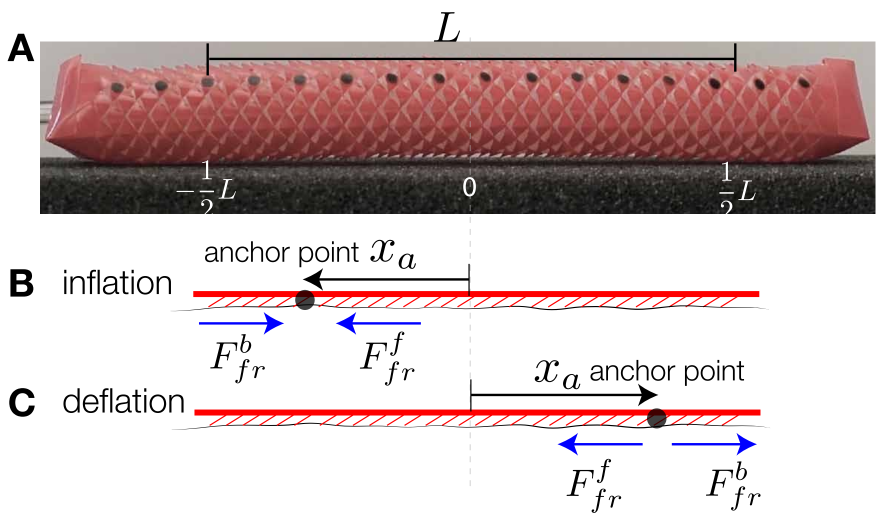

Figure S14. **Relation between the location of the anchor point and the fraction coefficients.** (**A**) Snapshot of our crawler. (**B**) Friction forces acting on the crawler during inflation. (**C**) Friction forces acting on the crawler during deflation.

As for the error of the model with respect to the experimental data, it is important to mention that in our simple analysis we assume quasi-static equilibrium and homogeneous deformations our experiments show that the deformation is not always homogeneous. Furthermore, an additional source of error is introduced during processing of the experimental data (i.e. when extracting the anchor point from the recorded experimental movies). To quantify the difference between the position of the anchor point as predicted by our model (x_a^m) and measured from our experiments (x_a^e), we calculate the normalized root-mean-square error

$$\text{NRMSD} = \frac{100}{x_{\max} - x_{\min}} \times \sqrt{\frac{\sum_1^n \left[\left(x_a^m \right)_i - \left(x_a^e \right)_i \right]^2}{n}} \Bigg/ \left(x_{\max} - x_{\min} \right) \qquad \text{(S7)}$$

where $x_{max} = L/2$ and $x_{min} = -L/2$ are respectively the maximum and minimum values for the position of the anchor point and $n = 8$ is the number of available data points. We find that NRMSD = 13.5%, 12.1%, 15.9% and 9.4% for the kirigami skins with triangular, circular, trapezoidal and mirrored triangular cuts, respectively.

Estimation of the total distance traveled by the crawlers

The total distance traveled by the crawlers, u_{tot}, when a total volume V_{tot} of air is supplied by cyclically inflating and deflating them between V_{max} and V_{min} can be calculated as

$$\frac{u_{tot}}{L_0} = N\left[-\int_{V_{\min}}^{V_{\max}}\left(\frac{x_a}{L}\right)\left(\frac{d\varepsilon}{dV}\right)dV + \int_{V_{\max}}^{V_{\min}}\left(\frac{x_a}{L}\right)\left(\frac{d\varepsilon}{dV}\right)dV\right] \quad \text{(S8)}$$

where $N = (V_{max} - V_{min})/V_{tot}$ are x_a denotes the position of the anchor point.

S4 Finite Element Simulations

In this Section, we present the results of Finite Element (FE) simulations conducted to study the effect of the cut shape on the stretchability of the corresponding kirigami skin. All simulations are conducted using the commercial package Abaqus¥Standard 6.14 (Dassault Systèmes). Moreover, in all analyses we consider flat sheets, discretize them with 3D shell elements (S4R) and model the cuts as seam cracks with duplicate overlapping nodes along the cuts. Finally, to reduce the computational cost and make sure the response of the system is not dominated by boundary effects, we investigate the response of infinite perforated flat sheets using a unit cell and periodic boundary conditions. Since here we are mostly interested in the response of the perforated sheet immediately after buckling (i.e. before the plastic deformation takes place), for this set of simulations we use a linear elastic material model (with E = 4.33 GPa and v = 0.4). All simulations consist of two steps: (*i*) we first use a linear perturbation analysis (*BUCKLE module in Abaqus) to identify the critical buckling mode; (*ii*) we then introduce a small imperfection (; 0.001l) in the form of the critical mode into the mesh to guide the post-buckling analysis. For this step we conduct dynamic implicit simulations (*DYNAMIC module in Abaqus) and to facilitate convergence, we introduce some artificial numerical damping.

In Fig. S15A-C we present the stress-strain curves obtained for unit cells with triangular, circular and trapezoidal cuts when stretched uniaxially (note that ε is the applied strain and s_k

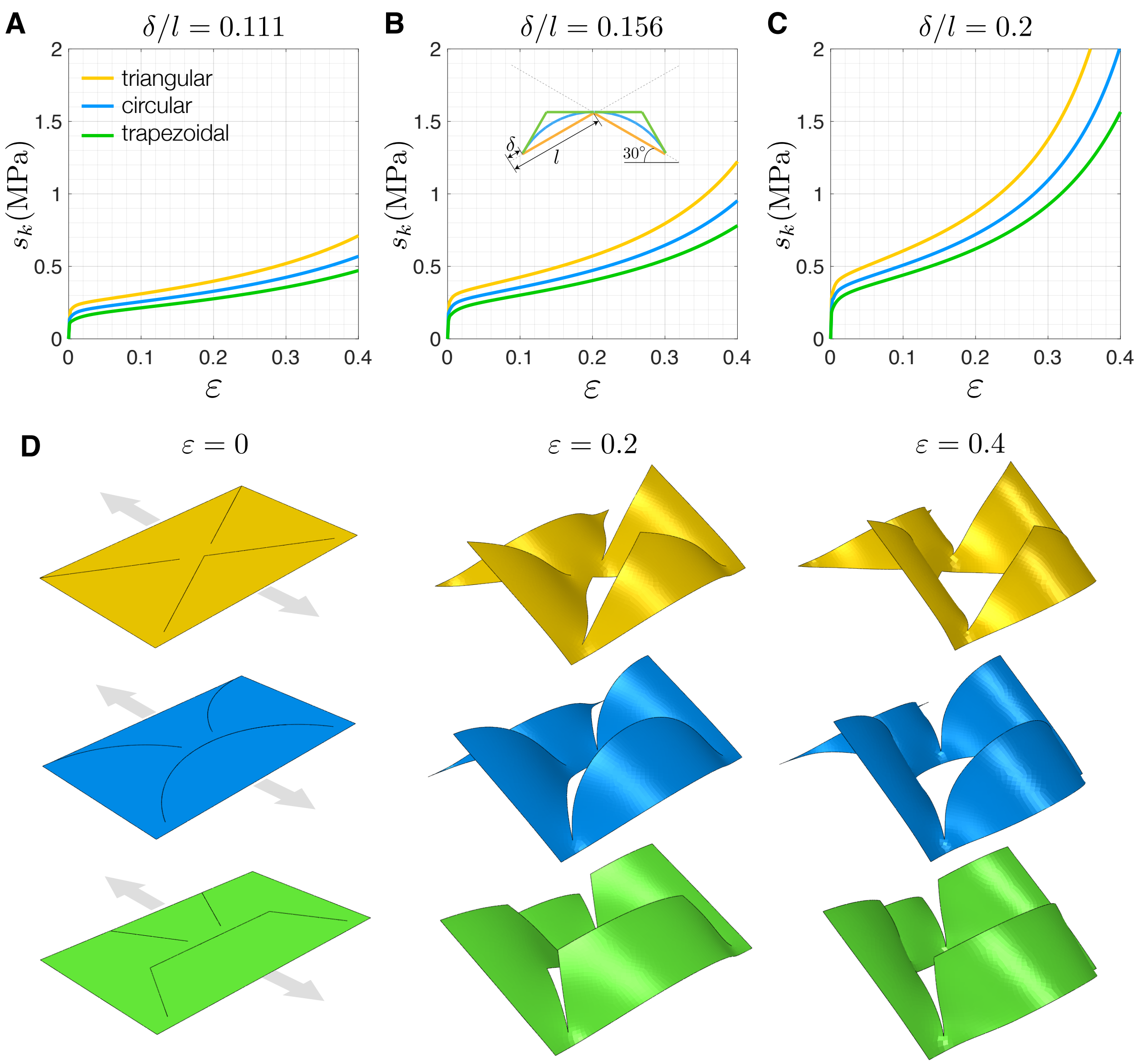

Figure S15. Finite-element simulations of kirigami unit cells. Stress-strain curves for unit cells with triangu- lar, circular and trapezoidal cuts for (**A**) *δ/l* = 0.111 (**B**) *δ/l* = 0.156 (**C**) *δ/l* = 0.2 (**D**) Snapshot of undeformed (ε = 0) and deformed configurations of unit cells for ε = 0.2 and ε = 0.4. Note that in our simulations we consider an elastic sheet with thickness t = 51μm, Young's modulus E = 4.33 GPa and Poisson's ratio v = 0.4.

is the measured nominal stress). Three different hinge widths are considered, i.e. δ/l = 0.111 (see Fig. S15A), 0.156 (see Fig. S15B) and 0.2 (see Fig. S15C). The simulations confirm the trends observed in experiments (see Fig. S6A) and indicate that the pattern with trapezoidal cut is the most stretchable. Moreover, as expected, they indicate that by increasing the hinge width, δ/l, the kirigami sheets become stiffer.

S5 Description of Supporting Movies

Movie S1. Rectilinear gait of a female Dumeril's boa. The snake actively tilts the ventral scales to increase frictional anisotropy and enhance anchoring (courtesy of H. Marvi and D. Hu).

Movie S2. A fiber-reinforced extending actuator is placed over a rough surface and is subjected to cyclic inflation/deflation. Since symmetry results in equal movement of both actuator ends during inflation and deflation, it does not move forward.

Movie S3. Assembly of a kirigami-skinned soft crawler.

Movie S4. Motion of the crawlers during six inflation cycles with $V \in [0,24]$ ml.

Movie S5. Motion of the crawlers when a total volume V_{tot} = 120 ml of air is supplied by cyclically inflating and deflating them between V_{max} = 24 ml and $V_{min} \in [0, V_{max}]$.

Movie S6. Fully untethered kirigami skinned crawlers with triangular, circular, and trapezoidal kirigami skins. Note that the rear part of the crawler is rigid and contains the control unit. Therefore, the pop-up of the portion of the skin that covers it is not that pronounced.

Movie S7. An untethered crawler with circular kirigami skin propels itself over asphalt.

Movie S8. An untethered crawler with trapezoidal kirigami skin climbs a concrete ramp.

Movie S9. An untethered crawler with triangular kirigami skin propels itself over rough stone. Note that the two vertical bands appearing on the kirigami skin during inflation are due to lighting, since in those locations the control unit beneath the skin is covered with black tape.

Movie S10. Motion of an untethered crawler with trapezoidal kirigami skin for P_{min} = 1, 4, 8, and 12 kPa and P_{max} = 16 kPa. The top left panel shows the real-time pressure inside the actuator, while the top right panel reports the position of the center of mass of the crawler over time.